Ground states and magnonics in orthogonally coupled symmetric all-antiferromagnetic junctions

Mei Li,[1] Bin Xi,[1] Wei He,[2] Yongjun Liu,[1] and Jie Lu[1,*]

[1]*College of Physics Science and Technology, Yangzhou University, Yangzhou 225002, People's Republic of China*

[2]*State Key Laboratory of Magnetism and Beijing National Laboratory for Condensed Matter Physics, Institute of Physics, Chinese Academy of Sciences, Beijing 100190, People's Republic of China*

(Received 29 November 2022; revised 16 February 2023; accepted 23 February 2023; published 8 March 2023)

In this paper, the rich ground-state structure of orthogonally coupled symmetric all-antiferromagnetic junctions with easy-plane anisotropy is reported. A spin reorientation process rather than the traditional spin flop (SF) occurs, resulting in a phase in which Néel vectors preserve the mirror-reflection symmetry (termed MRS phase). The phase transitions in the ground state between SF and MRS phases can be either first or second order. After disturbed by external stimuli, magnons with different parities emerge. For in-plane dc fields, no couplings between magnons occur. When dc fields become oblique, coherent couplings between magnons with opposite parity emerge, leading to anticrossings in resonance frequencies. However, self-hybridization among magnons with the same parity never happens. More interestingly, spin waves based on MRS phases are linearly polarized and their polarization directions can be fine controlled.

DOI: 10.1103/PhysRevB.107.094407

I. INTRODUCTION

All-antiferromagnetic junctions, such as $Fe_2O_3/Cr_2O_3/Fe_2O_3$, have been recently proposed to be candidates for practical antiferromagnetic spintronics and magnonics with ultrahigh-density integration [1]. Different from the well-know synthetic antiferromagnets [2–27] in which the collinear interlayer coupling between ferromagnetic sublayers is the Ruderman-Kittel-Kasuya-Yosida interaction mediated by electrons [28–30], the coupling between two antiferromagnetic Fe_2O_3 sublayers in all-antiferromagnetic junctions is claimed to be bridged by the nonuniform domain-wall state in Cr_2O_3 spacers. In recent experiments, the double-peak structure in spin Hall magnetoresistance (SMR) [31–35] signals of asymmetric $Fe_2O_3/Cr_2O_3/Fe_2O_3$ junctions are explained by the orthogonal coupling between the Néel vectors in the two outermost Fe_2O_3 layers with different thickness. However, the detailed magnetic ground states of these junctions have not yet been provided. In addition, magnon-magnon coupling and its resulting modification to the eigenfrequencies and eigenvectors need to be revealed. In this paper, we focus on the simplified version, that is, symmetric all-antiferromagnetic junctions where the two outermost sublayers are made from the same materials with the same thickness. The magnetic ground states and coherent magnonics in these systems constitute the main contents of this paper.

II. MODEL AND METHODS

In most existing literature, Lagrangians of two-sublattice antiferromagnets are written in terms of Néel vectors, in which the lowest nonvanishing kinetic terms are obtained by expanding the vector potentials (from Berry phase) to the first order of the total magnetization $\mathbf{m}$ of the unit cell in antiferromagnets (slave variable of Néel vector) [36–38]. This is based on the assumption of $|\mathbf{m}| \ll 1$ and is generally true for magnetic states not far from the antiferromagnetic ground state ($\mathbf{m} = 0$) and the corresponding magnonics based on them. However, in this paper we focus on the entire evolution process of a magnetic ground state under uniform and static external fields during which the ground state of magnetic materials varies from antiferromagnetic to ferromagnetic. The assumption of $|\mathbf{m}| \ll 1$ gradually fails, hence existing forms of the antiferromagnet Lagrangian may be insufficient. To correctly obtain the magnetic ground state and understand the corresponding magnonics, we have to revert to the original description of antiferromagnets with the respective unit magnetization of each sublattice and the corresponding coupled Landau-Lifshitz-Gilbert (LLG) equations [39]. When identifying magnetic phases and phase transitions (PTs), as well as the corresponding physical quantities (for example, the SMR signal), we shift to the Néel-vector language to provide up-to-date descriptions and explanations on the unique behaviors of these all-antiferromagnetic junctions.

Generally, the antiferromagnetic Cr_2O_3 spacer possesses a spin-flop (SF) field [40] higher than 6 T [41,42], which is much larger than that of Fe_2O_3 (a few thousand Oe) [43,44]. Therefore, in our analytics the two identical antiferromagnetic outermost Fe_2O_3 sublayers (denoted as A and B) are assumed to have the simplest easy-plane anisotropy with the hard axis along the surface normal (z axis), as shown in Fig. 1(a). In each layer, the magnetic energy density is

$$\frac{\mathcal{E}_s[\mathbf{m}_{i,1(2)}]}{\mu_0} = M_s H_E \mathbf{m}_{i,1}\cdot\mathbf{m}_{i,2} + \frac{M_s H_K}{2}\left(\mathrm{m}_{i,1z}^2 + \mathrm{m}_{i,2z}^2\right) - M_s(\mathbf{m}_{i,1}+\mathbf{m}_{i,2})\cdot\mathbf{H}_{\mathrm{ext}}, \quad i = A, B, \tag{1}$$

where $\mathbf{m}_{i,1}$ and $\mathbf{m}_{i,2}$ are the unit vectors of the two sublattices in the ith antiferromagnetic sublayer with the same saturation magnetization M_s and mutual exchange field $H_E(>0)$,

*lujie@yzu.edu.cn

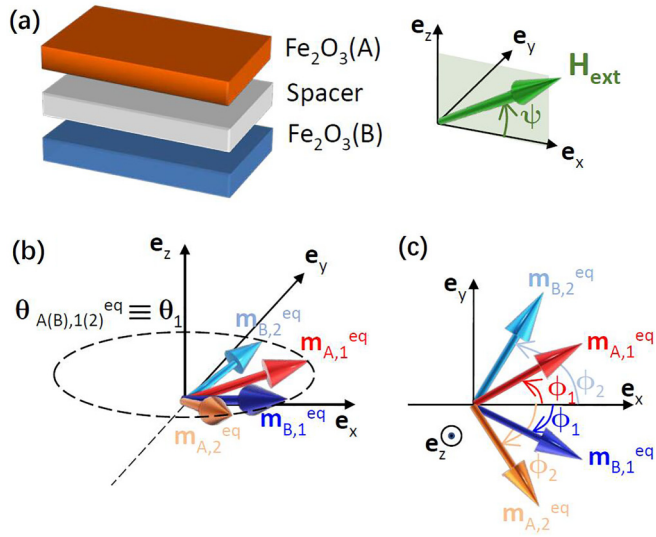

FIG. 1. (a) Sketch of an orthogonally coupled symmetric all-antiferromagnetic junction with the same thickness in two outermost Fe_2O_3 sublayers (denoted as A and B). $\mathbf{e}_z$ is along surface normal, $\mathbf{e}_y \parallel \mathbf{e}_z \times \mathbf{H}_{\rm ext}$, and $\mathbf{e}_x = \mathbf{e}_y \times \mathbf{e}_z$, in which the external oblique dc field reads $\mathbf{H}_{\rm ext} = H_0(\cos\psi\mathbf{e}_x + \sin\psi\mathbf{e}_z)$. (b) The four equilibrium unit magnetization vectors in two Fe_2O_3 sublayers are denoted as $\mathbf{m}^{\rm eq}_{A(B),1(2)}$ and all fall onto the same latitude circle $\theta = \theta_1$. Meanwhile, $\mathbf{m}^{\rm eq}_{A,1}$ and $\mathbf{m}^{\rm eq}_{B,1}$ ($\mathbf{m}^{\rm eq}_{A,2}$ and $\mathbf{m}^{\rm eq}_{B,2}$) are symmetric about the xz plane. (c) Vertical view of (b). The azimuthal angle of $\mathbf{m}^{\rm eq}_{A,1}$ ($\mathbf{m}^{\rm eq}_{B,1}$) is ϕ_1 ($-\phi_1$), while that for $\mathbf{m}^{\rm eq}_{A,2}$ ($\mathbf{m}^{\rm eq}_{B,2}$) is $-\phi_2$ (ϕ_2).

$H_K(>0)$ is the anisotropy field along hard axis, $\mathbf{H}_{\rm ext}$ denotes the external dc field, and μ_0 is the vacuum permeability.

We then neglect the details of spacers and phenomenologically introduce the orthogonal coupling between two outermost sublayers. Originally, the interlayer orthogonal coupling is expressed as $\mathcal{E}_{\rm c} = J'(\mathbf{n}_A \cdot \mathbf{n}_B)^2/2 = J'\cos^2\theta_{AB}/2$, in which $J' > 0$ and $\mathbf{n}_i \equiv (\mathbf{m}_{i,1} - \mathbf{m}_{i,2})/|\mathbf{m}_{i,1} - \mathbf{m}_{i,2}|$ are the Néel vectors of each antiferromagnetic sublayer with θ_{AB} being the angle spanned by them. However, this format of $\mathcal{E}_{\rm c}$ is inconvenient in deducing the equilibrium ground state and dynamic response of magnetization vectors. Considering the fact that in antiferromagnets, $\mathbf{n}_i \perp \mathbf{m}_i(\equiv \mathbf{m}_{i,1} + \mathbf{m}_{i,2})$, an equivalent format is provided as

$$\mathcal{E}_{\rm c} = \frac{J}{2}(\mathbf{m}_A \cdot \mathbf{m}_B)^2, \tag{2}$$

with $J(>0)$ denoting the coupling strength. Combing all these components, the total magnetic energy of this junction reads

$$E_{\rm tot} = \sum_{i=A,B} \mathcal{E}_{\rm s}[\mathbf{m}_{i,1}, \mathbf{m}_{i,2}] \cdot (S_0 d_0) + \mathcal{E}_{\rm c} \cdot S_0, \tag{3}$$

with S_0 and d_0 being the projection area and thickness of each outermost sublayer, respectively. In macrospin assumption, the effective field of a single-domain volume with unit magnetization $\mathbf{m}$, projection area S, and thickness d is defined as $\mathbf{H}_{\rm eff} = -\mu_0^{-1}\delta E_{\rm tot}/\delta(M_s S d\mathbf{m})$.

The dynamics of $\mathbf{m}_{A(B),1(2)}$ are described by the coupled LLG equations

$$\frac{d\mathbf{m}_{A(B),1(2)}}{dt} = -\gamma\mathbf{m}_{A(B),1(2)} \times \mathbf{H}^{A(B),1(2)}_{\rm eff} + \mathbf{T}_{A(B),1(2)}, \tag{4}$$

where $\mathbf{T}_{A(B),1(2)}$ includes torques from both damping and external dc fields, $\gamma = \mu_0\gamma_e$, with γ_e being electron gyromagnetic ratio. The effective field $\mathbf{H}^{A,1}_{\rm eff}$ reads

$$\mathbf{H}^{A,1}_{\rm eff} = \mathbf{H}_{\rm ext} - H_E\mathbf{m}_{A,2} - H_K m_{A,1z}\mathbf{e}_z - H_p(\mathbf{m}_A \cdot \mathbf{m}_B)\mathbf{m}_B, \tag{5}$$

with $H_p \equiv J/(\mu_0 M_s d)$, the other three effective fields can be obtained by performing $A \leftrightarrow B$ and $1 \leftrightarrow 2$. These are all we need to proceed with our investigation.

III. GROUND STATES AND PHASE TRANSITIONS

We consider a general $\mathbf{H}_{\rm ext}$ with a strength H_0 and polar angle $\frac{\pi}{2} - \psi$ with respect to $\mathbf{e}_z$ [see Fig. 1(a)]. After defining $\mathbf{e}_y \parallel \mathbf{e}_z \times \mathbf{H}_{\rm ext}$ and $\mathbf{e}_x = \mathbf{e}_y \times \mathbf{e}_z$, $\mathbf{H}_{\rm ext} = H_0(\cos\psi\mathbf{e}_x + \sin\psi\mathbf{e}_z)$. The equilibrium magnetization vectors (emphasized by a superscript $^{\rm eq}$) in sublayers A and B should be symmetric about the xz plane. In view of this, we define the following polar and azimuthal angles: $\mathbf{m}^{\rm eq}_{A(B),1}[\mathbf{m}^{\rm eq}_{A(B),2}]$ has the polar angle $\theta_1(\theta_2)$ and azimuthal angle $\pm\phi_1(\mp\phi_2)$. The static condition requires $d\mathbf{m}_{A(B),1(2)}/dt = 0$ and $\mathbf{T}_{A(B),1(2)} = 0$. This results in (i) $\theta_1 = \theta_2$, that is, $\mathbf{m}_{A(B),1(2)}$ all lie in the same latitude circle [see Fig. 1(b)], hence $\mathbf{n}^{\rm eq}_A$ and $\mathbf{n}^{\rm eq}_B$ always reside in the xy plane; and (ii) the central equality of this paper,

$$\begin{aligned} &h(\cos\psi\mathbf{e}_x + \sin\psi\mathbf{e}_z) \\ &\quad = \mathbf{m}^{\rm eq}_A + p\big(\mathbf{m}^{\rm eq}_A \cdot \mathbf{m}^{\rm eq}_B\big)\mathbf{m}^{\rm eq}_B + k\cos\theta_1\mathbf{e}_z, \end{aligned} \tag{6}$$

where $h \equiv H_0/H_E$, $p \equiv H_p/H_E$, and $k \equiv H_K/H_E$ are all positive. This equality is very important and will be used to (i) calculate $\mathbf{m}^{\rm eq}_{A(B),1(2)}$ (i.e., θ_1 and $\phi_{1(2)}$) and (ii) simplify the dynamic equations for spin waves.

Two extreme circumstances are first examined: zero-field and high-enough-field cases. In the absence of external fields ($h = 0$), due to the lack of in-plane anisotropy the ground state of this symmetric all-antiferromagnetic junction is a cruciferae state, namely, $\mathbf{m}_{A,1}$, $\mathbf{m}_{B,1}$, $\mathbf{m}_{A,2}$, and $\mathbf{m}_{B,2}$ are successively arranged clockwise in the xy plane at $\pi/2$ intervals (thus $\theta^{\rm eq}_{AB} = \pi/2$), taking the most advantage of energy gain from the orthogonal coupling. On the other hand, there always exists an upper limit of external field strength $h^{\rm FM} \equiv [\cos^2\psi/(8p+2)^2 + \sin^2\psi/(8p+k+2)^2]^{-1/2}$. Above it, the system falls into the ferromagnetic saturated state (FM phase), which means $\mathbf{m}_{A(B),1(2)} \equiv \mathbf{m}^{\rm FM} = \sin\theta^{\rm FM}_1\mathbf{e}_x + \cos\theta^{\rm FM}_1\mathbf{e}_z$, with $\theta^{\rm FM}_1$ satisfying

$$h\cos\left(\theta^{\rm FM}_1 + \psi\right) + (k/2)\sin 2\theta^{\rm FM}_1 = 0. \tag{7}$$

The presence of k leads to $\pi/2 - \psi < \theta^{\rm FM}_1 < \pi/2$, meaning that $\mathbf{m}^{\rm FM}$ lies between $\mathbf{H}_{\rm ext}$ and $\mathbf{e}_x$. Now $\mathbf{n}^{\rm eq}_A = \mathbf{n}^{\rm eq}_B = 0$, hence θ_{AB} has no definition in FM phase.

For $0 < h < h^{\rm FM}$, the system exhibits the complex ground state and PTs in it, as illustrated in Figs. 2(a) and 2(b). The orthogonal coupling strength p strongly affects the equilibrium magnetization layout. For weak orthogonal couplings ($0 < p < 1/4$), before saturation the system always falls into the SF ground state with the polar and azimuthal angles

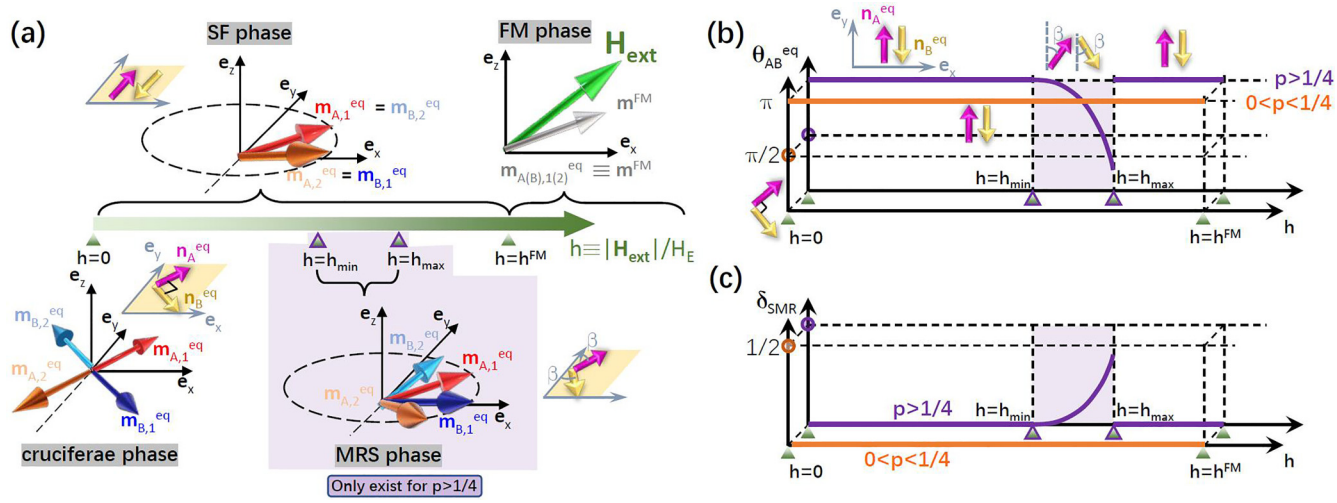

FIG. 2. (a) Ground-state evolution of orthogonally coupled symmetric all-antiferromagnetic junctions as the external dc field increases. In various phases, red (orange) and blue (cyan) arrows, respectively, denote $\mathbf{m}_{A,1(2)}$ and $\mathbf{m}_{B,1(2)}$, while magenta (gold) arrow indicates the Néel vector $\mathbf{n}_A^{\rm eq}$ ($\mathbf{n}_B^{\rm eq}$). At $h=0$, $\mathbf{m}_{A(B),1(2)}$ evenly spread in xy plane at $\pi/2$ interval (cruciferae phase). Hence $\mathbf{n}_A^{\rm eq}\perp\mathbf{n}_B^{\rm eq}$. For $h\geqslant h^{\rm FM}$, $\mathbf{m}_{A(B),1(2)}\equiv\mathbf{m}^{\rm FM}$, thus the system falls into the FM phase. When $0<h<h^{\rm FM}$, SF phase with $\mathbf{m}_{A,1}^{\rm eq}=\mathbf{m}_{B,2}^{\rm eq}$ and $\mathbf{m}_{A,2}^{\rm eq}=\mathbf{m}_{B,1}^{\rm eq}$ always bears the lowest magnetic energy for $0<p<1/4$. While for $p>1/4$, MRS phase emerges and acquires the lowest energy for $h\in[h_{\rm min},h_{\rm max}]\subset(0,h^{\rm FM})$. (b) Variation of $\theta_{AB}^{\rm eq}$ (the angle between $\mathbf{n}_A^{\rm eq}$ and $\mathbf{n}_B^{\rm eq}$) with the external fields. Orange line (purple curve) is for the case with $0<p<1/4$ ($p>1/4$). The PT (SF process) at $h=0$ is always first order as $\theta_{AB}^{\rm eq}$ changes abruptly from $\pi/2$ to π. For $p>1/4$, the light-purple area denotes the novel MRS phase. The PT between SF and MRS phases at $h=h_{\rm min}$ ($h_{\rm max}$) is second (first) order. (c) Normalized SMR signals as functions of the external field h. Orange line (purple curve) is for the case with $0<p<1/4$ ($p>1/4$).

satisfying

$$8pk^2\cos^5\theta_1-16phk\sin\psi\cos^4\theta_1+(8ph^2+k^3+2k^2)\cos^3\theta_1-(3k+4)hk\sin\psi\cos^2\theta_1$$
$$+\,(3k+2)h^2\sin^2\psi\cos\theta_1-h^3\sin^3\psi=0,$$
$$\cos\phi_1=\cos\phi_2=\frac{h\cos\psi\cos\theta_1}{(h\sin\psi-k\cos\theta_1)\sin\theta_1}. \tag{8}$$

In fact, this SF phase is the counterpart of the spin-flopped state in a single antiferromagnetic layer (with zero in-plane anisotropy) since the orthogonal coupling now is too weak to affect the magnetization layout. Now $\mathbf{n}_A^{\rm eq}=\mathbf{e}_y$ and $\mathbf{n}_B^{\rm eq}=-\mathbf{e}_y$, leading to $\theta_{AB}^{\rm eq}=\pi$. Correspondingly, the PT at $h=0$ is first order. At $h=h^{\rm FM}$, Eq. (8) continuously converges to Eq. (7), leading to a second-order PT therein.

More interestingly, for large enough orthogonal coupling ($p>1/4$), a new phase acquires lower energy than the SF phase for $h\in[h_{\rm min},h_{\rm max}]\subset(0,h^{\rm FM})$, with $h_{\rm min}\equiv(p^{-1/2}/2)/\sqrt{\cos^2\psi/16+\sin^2\psi/(k+4)^2}$ and $h_{\rm max}\equiv\sqrt{1/2+1/(8p)}/\sqrt{\cos^2\psi/16+\sin^2\psi/(k+4)^2}$. The polar and azimuthal angles are

$$\cos\theta_1=\frac{h}{k+4}\sin\psi,\quad \phi_1=\alpha-\beta,\quad \phi_2=\alpha+\beta,$$
$$\text{with}\quad \alpha\equiv\arccos\frac{1}{2}\sqrt{\frac{\frac{\cos^2\psi}{2}+\frac{4\sin^2\psi}{(k+4)^2}-\frac{1}{h^2p}}{\frac{1}{h^2}-\frac{\sin^2\psi}{(k+4)^2}}},$$
$$\beta\equiv\arccos\sqrt{\frac{\frac{\cos^2\psi}{4}}{\frac{\cos^2\psi}{2}+\frac{4\sin^2\psi}{(k+4)^2}-\frac{1}{h^2p}}}, \tag{9}$$

where we have assumed $|\phi_1|<\phi_2<\pi-|\phi_1|$ without losing generality. Then $\mathbf{n}_A^{\rm eq}=\sin\beta\mathbf{e}_x+\cos\beta\mathbf{e}_y$ and $\mathbf{n}_B^{\rm eq}=\sin\beta\mathbf{e}_x-\cos\beta\mathbf{e}_y$. Correspondingly, $\theta_{AB}^{\rm eq}=\pi-2\beta=\pi-(\phi_2-\phi_1)$. This phase comes from the competition between interlayer orthogonal and intralayer antiferromagnetic couplings, however, it preserves the mirror-reflection symmetry (MRS) about the xz plane. We hereby denote it as the MRS phase. It coincides with the SF phase at $h=h_{\rm min}$ since $\beta(h_{\rm min})=0$ (hence $\phi_1=\phi_2$), which implies a second-order PT herein ($\theta_{AB}^{\rm eq}=\pi$ on both sides of $h_{\rm min}$). However, when h increases and approaches $h_{\rm max}$, $\alpha\to0$ leading to $-\phi_1\approx\phi_2\to\beta(h_{\rm max})$ with $\beta(h_{\rm max})\equiv\arccos\sqrt{(4p+1)/[8p+16(4p-1)\tan^2\psi/(k+4)^2]}<\pi/2$. Hence, $\theta_{AB}^{\rm eq}=\pi-2\beta(h_{\rm max})>0$ [see Fig. 2(b)]. When h slightly exceeds $h_{\rm max}$, the ground state abruptly moves back to the SF phase with $\theta_{AB}^{\rm eq}=\pi$, leading to a first-order PT at $h_{\rm max}$.

To obtain an intuitive impression on the SF and MRS phases, as well as PTs in the system's ground state, we perform energetic calculations with typical parameters ($\psi=\pi/10$, $k=1$) and the results are illustrated in Fig. 3. We take $p=0.15$ and $p=0.45$ as two typical examples. For each p, the equilibrium polar and azimuthal angles are solved from Eq. (8) for SF phase and Eq. (9) for MRS phase (when exists).

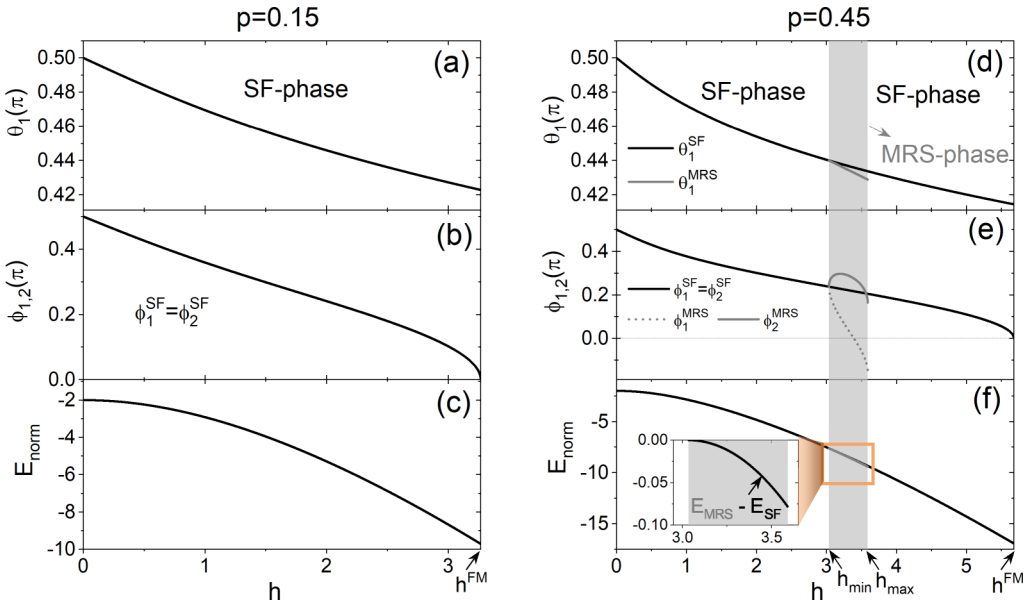

FIG. 3. Magnetic phases of orthogonally coupled symmetric all-antiferromagnetic junctions with $k = 1$ and two typical p under static magnetic fields with fixed $\psi = \pi/10$. (a)–(c) Polar angle θ_1, azimuthal angles $\phi_{1,2}$, and normalized energy $E_{\rm norm}$ for $p = 0.15$. Only SF phase is present. (d)–(f) Counterparts for $p = 0.45$. SF phase persists, while MRS phase emerges for $h \in [h_{\rm min}, h_{\rm max}]$ and is emphasized by light-gray areas. Data for SF (MRS) phase are plotted by black (gray) curves. The inset of (f) provides $E^{\rm MRS}_{\rm norm} - E^{\rm SF}_{\rm norm}$.

Then the corresponding normalized energy density, $E_{\rm norm} \equiv E_{\rm tot}/(\mu_0 M_s H_E S_0 d_0)$, is calculated for $0 < h < h^{\rm FM}$. For $p = 0.15(< 1/4)$, $h^{\rm FM} = 3.2661$. The polar angle θ_1, azimuthal angles $\phi_{1,2}$ and normalized magnetic energy $E_{\rm norm}$ of SF phase are, respectively, plotted by solid curves in Figs. 3(a)–3(c). The MRS phase never appears, thus the ground state of the system always falls into the SF phase for all values of h. For $p = 0.45(> 1/4)$, $h^{\rm FM} = 5.6764$. Besides the ever-present SF phase, now the MRS phase emerges when $h_{\rm min} \leqslant h \leqslant h_{\rm max}$ with $h_{\rm min} = 3.0340$ and $h_{\rm max} = 3.5900$, and is emphasized by light-gray areas in Figs. 3(d)–3(f). Correspondingly, the polar and azimuthal angles as well as normalized magnetic energy of the SF (MRS) phase are depicted by black (gray) curves. For clearance, the inset of Fig. 3(f) shows the difference of normalized energy ($E^{\rm MRS}_{\rm norm} - E^{\rm SF}_{\rm norm}$), which is two orders of magnitude smaller than $E^{\rm SF}_{\rm norm}$. Clearly, the ground state of the system changes from the SF to MRS phase for $h_{\rm min} \leqslant h \leqslant h_{\rm max}$. In addition, the PT at $h_{\rm min} = 3.0340$ ($h_{\rm max} = 3.5900$) is second order (first order).

This MRS phase is essential for the nonzero SMR signals under finite dc fields even in the absence of in-plane magnetic anisotropy for symmetric all-antiferromagnetic junctions with strong enough orthogonal couplings. Suppose a heavy-metal cap layer (for example, Pt), through which a charge current passes in $+\mathbf{e}_x$ direction, is attached onto a symmetric all-antiferromagnetic junction under $\mathbf{H}_{\rm ext} = hH_E(\cos\psi\mathbf{e}_x + \sin\psi\mathbf{e}_z)$. The spin polarization generated by the spin Hall effect of the heavy-metal caplayer is then along the y axis. Generally, when Néel vectors of the outermost antiferromagnetic sublayers ($\mathbf{n}^{\rm eq}_A$ and $\mathbf{n}^{\rm eq}_B$) are parallel (perpendicular) to the spin polarization, the system has a comparatively low (high) resistance. In general, we use

$$\delta_{\rm SMR} = 1 - \frac{\left(\mathbf{n}^{\rm eq}_A \cdot \mathbf{e}_y\right)^2 + \left(\mathbf{n}^{\rm eq}_B \cdot \mathbf{e}_y\right)^2}{2} \tag{10}$$

to describe the normalized SMR signal of this junction, as illustrated in Fig. 2(c).

For small orthogonal coupling ($0 < p < 1/4$), $\mathbf{n}^{\rm eq}_{A(B)}$ in the SF phase always lie in the y axis for nonzero h, leading to a plateau with $\delta^{\rm SF}_{\rm SMR} = 0$ [see orange line in Fig. 2(c)]. The only peak with the height of $1/2$ occurs at $h = 0$ where the cruciferae phase emerges. While for large enough orthogonal coupling ($p > 1/4$), in the MRS phase one has $\delta^{\rm MRS}_{\rm SMR} = \sin^2\beta$ which is strengthened from 0 to

$$\delta^{\rm MRS}_{\rm SMR}(\beta_{\rm max}) = \frac{1 + \frac{16\tan^2\psi}{(k+4)^2}}{\frac{8p}{4p-1} + \frac{16\tan^2\psi}{(k+4)^2}} \tag{11}$$

as h increases from $h_{\rm min}$ to $h_{\rm max}$. The normalized SMR signal rapidly decreases to zero as h exceeds $h_{\rm max}$. In real junctions, these abrupt peaks will be broadened due to the finite distribution of the anisotropy in sublayers, as well as the possible magnetic impurities therein.

This MRS-phase-induced resistance peak is unique for symmetric all-antiferromagnetic junctions since $\mathbf{n}^{\rm eq}_{A(B)}$ lie symmetrically about $xz-$plane. It differs from the resistance peaks (i) and (iii) in Figs. 2(d) and 2(e) from Ref. [1], at which $\mathbf{n}^{\rm eq}_A$ and $\mathbf{n}^{\rm eq}_B$ are, respectively, along $\mathbf{e}_x$ and $\mathbf{e}_y$. In addition, it discriminates from the negative SMR signal of a single antiferromagnetic Fe_2O_3 layer (see Figs. 2(a) and 2(b) from Ref. [1]), where the (only) resistance peak appears at $H < 0$ ($H > 0$) when in-plane external field with strength H sweeping from positive to negative (negative to positive). The reasons are twofold. On one hand, the MRS-phase-induced resistance peak survives even in the absence of in-plane anisotropy while that of the single Fe_2O_3 layer relies on it. On the other hand, the SMR peak occurs in the MRS phase which emerges for $h \in [h_{\rm min}, h_{\rm max}] \subset (0, h^{\rm FM})$, thus is a post-SF effect taking place under a relatively large external field strength (around $h_{\rm max}$). The latter reason also helps us

to exclude the interlayer coupling between Fe_2O_3 sublayers in $Fe_2O_3/Al_2O_3/Fe_2O_3$ junctions as shown in Fig. S19 from the Supplementary Note of Ref. [1]. At last, the experimental SMR data of the symmetric $Fe_2O_3/NiO/Fe_2O_3$ junction in Fig. S18 from the same work did not show strong signs of a MRS peak. This possibly comes from the fact that NiO has a not-high-enough SF field [45,46] thus making the data contain too many physical processes.

At the end of this section, we define several symmetry operators for further usage. The first one is the mirror reflection operator $\mathbb{M}_{xz}$ which converts a vector $\mathbf{U} = U_x\mathbf{e}_x + U_y\mathbf{e}_y + U_z\mathbf{e}_z$ to $\mathbb{M}_{xz}\mathbf{U} = U_x\mathbf{e}_x - U_y\mathbf{e}_y + U_z\mathbf{e}_z$. $\mathbb{M}_{xz}$ is used to simplify the dynamical equations of spin waves in the MRS phase under oblique dc fields (to be delivered in Sec. IV.C.1), but the polarization of spin waves will be reversed. Next, we define two rotational operations which preserve the polarization of spin waves. Since $\mathbb{M}_{xz}\mathbf{m}^{\rm eq}_{A,1(2)} = \mathbf{m}^{\rm eq}_{B,1(2)}$, the planes expanded by $(\mathbf{m}^{\rm eq}_{A,1}, \mathbf{m}^{\rm eq}_{B,1})$ and $(\mathbf{m}^{\rm eq}_{A,2}, \mathbf{m}^{\rm eq}_{B,2})$ both intersect with the xy plane on the y axis. We choose $\mathbf{e}_{x'} \parallel \mathbf{m}^{\rm eq}_{A,1} + \mathbf{m}^{\rm eq}_{B,1}$ and $\mathbf{e}_{x''} \parallel \mathbf{m}^{\rm eq}_{A,2} + \mathbf{m}^{\rm eq}_{B,2}$. Correspondingly, the angle between $\mathbf{e}_{x'}$ ($\mathbf{e}_{x''}$) and $\mathbf{e}_x$ is defined as χ (ξ). Meantime, the angle between $\mathbf{e}_{x'}$ and $\mathbf{m}^{\rm eq}_{A,1}$ ($\mathbf{e}_{x''}$ and $\mathbf{m}^{\rm eq}_{A,2}$) is ϵ (η). Then we have $\tan\chi = \cot\theta_1/\cos\phi_1$, $\tan\xi = \cot\theta_1/\cos\phi_2$, $\sin\epsilon = \sin\theta_1\sin\phi_1$, and $\sin\eta = \sin\theta_1\sin\phi_2$. Consequently, $\mathbb{C}_{2x'}$ ($\mathbb{C}_{2x''}$) is defined as the rotation operator which rotates vectors around $+\mathbf{e}_{x'}$ ($+\mathbf{e}_{x''}$) by 180° while preserving the polarization of spin waves. With these ground states and operators, in the next sections we proceed to dynamical response of magnetization vectors to external stimuli.

IV. MAGNONICS

A. General framework

Suppose a RF magnetic field with a frequency $f = \omega/2\pi$ is induced by some antenna and then excites spin waves to propagate in the whole junction. The magnetization vectors $\mathbf{m}_{A(B),1(2)}$ slightly deviate from their equilibrium orientations $\mathbf{m}^{\rm eq}_{A(B),1(2)}$ and begin to vibrate with the same frequency f. Consequently, they are expanded as $\mathbf{m}_{A(B),1(2)} = \mathbf{m}^{\rm eq}_{A(B),1(2)} + \delta\mathbf{m}_{A(B),1(2)}e^{i\omega t}$. After defining $\Omega \equiv \omega/(\gamma H_E)$ and neglecting $\mathbf{T}_{A(B),1(2)}$, we obtain the following central vectorial equations for $\delta\mathbf{m}_{A(B),1(2)}$ with the help of Eq. (6):

$$\begin{aligned} i\Omega\delta\mathbf{m}_{A(B),1(2)} = \mathbf{m}^{\rm eq}_{A(B),1(2)} \times \big\{&(\delta\mathbf{m}_{A(B),1} + \delta\mathbf{m}_{A(B),2}) + k(\delta\mathbf{m}_{A(B),1(2)}\cdot\mathbf{e}_z)\mathbf{e}_z + p\big(\mathbf{m}^{\rm eq}_A\cdot\mathbf{m}^{\rm eq}_B\big)(\delta\mathbf{m}_{B(A),1} + \delta\mathbf{m}_{B(A),2}) \\ &+ p\big[(\delta\mathbf{m}_{A,1} + \delta\mathbf{m}_{A,2})\cdot\mathbf{m}^{\rm eq}_B + (\delta\mathbf{m}_{B,1} + \delta\mathbf{m}_{B,2})\cdot\mathbf{m}^{\rm eq}_A\big]\mathbf{m}^{\rm eq}_{B(A)}\big\}, \end{aligned} \tag{12}$$

which are the central equations for coherent magnonics in orthogonally coupled symmetric all-antiferromagnetic junctions.

B. In-plane-dc-field case

1. Reformation of dynamical equations

For in-plane dc fields ($\psi = 0$), $\theta_1 = \pi/2$, thus $\mathbf{m}^{\rm eq}_{A(B),1(2)}$ all reside in the xy plane. Consequently, $\mathbf{e}_{x'} = \mathbf{e}_{x''} = \mathbf{e}_x$, leading to $\mathbb{C}_{2x'} = \mathbb{C}_{2x''} = \mathbb{C}_{2x}$. We then introduce $\delta\mathbf{m}^{\pm}_{1(2)} \equiv \delta\mathbf{m}_{A,1(2)} \pm \mathbb{C}_{2x}\delta\mathbf{m}_{B,1(2)}$ as the spin wave components with even (+) and odd (–) parities under $\mathbb{C}_{2x}$. Hence Eq. (12) becomes

$$\begin{aligned} i\Omega\delta\mathbf{m}^{+}_{1(2)} =& \mathbf{m}^{\rm eq}_{A,1(2)} \times \big\{(\delta\mathbf{m}^{+}_1 + \delta\mathbf{m}^{+}_2) + k(\delta\mathbf{m}^{+}_{1(2)}\cdot\mathbf{e}_z)\mathbf{e}_z \\ &+ p\big(\mathbf{m}^{\rm eq}_A\cdot\mathbf{m}^{\rm eq}_B\big)\mathbb{C}_{2x}(\delta\mathbf{m}^{+}_1 + \delta\mathbf{m}^{+}_2) \\ &+ 2p\big[\mathbf{m}^{\rm eq}_B\cdot(\delta\mathbf{m}^{+}_1 + \delta\mathbf{m}^{+}_2)\big]\mathbf{m}^{\rm eq}_B\big\}, \\ i\Omega\delta\mathbf{m}^{-}_{1(2)} =& \mathbf{m}^{\rm eq}_{A,1(2)} \times \big\{(\delta\mathbf{m}^{-}_1 + \delta\mathbf{m}^{-}_2) + k(\delta\mathbf{m}^{-}_{1(2)}\cdot\mathbf{e}_z)\mathbf{e}_z \\ &- p\big(\mathbf{m}^{\rm eq}_A\cdot\mathbf{m}^{\rm eq}_B\big)\mathbb{C}_{2x}(\delta\mathbf{m}^{-}_1 + \delta\mathbf{m}^{-}_2)\big\}. \end{aligned} \tag{13}$$

In the local coordinate system $(\mathbf{e}^{1(2)}_{\mathbf{m}} \equiv \mathbf{m}^{\rm eq}_{A,1(2)}, \mathbf{e}^{1(2)}_{\phi} \equiv \mathbf{e}_z \times \mathbf{e}^{1(2)}_{\mathbf{m}}, \mathbf{e}_z)$, we decompose $\delta\mathbf{m}^{\pm}_{1(2)}$ as $\delta\mathbf{m}^{\pm}_{1(2)} = \delta m^{\pm}_{1(2),\phi}\mathbf{e}^{1(2)}_{\phi} + \delta m^{\pm}_{1(2),z}\mathbf{e}_z$. Then Eq. (13) is decoupled into two 4×4 matrix equations. After diagonalizing them, the eigenfrequencies and eigenvectors of spin waves with different parities are obtained.

2. Subspace with even parity under $\mathbb{C}_{2x}$

The coupled vectorial equations with even parity are transformed into their matrix-form counterpart:

$$\Omega\begin{pmatrix}\delta m^{+}_{1,\phi}\\ \delta m^{+}_{2,\phi}\\ i\delta m^{+}_{1,z}\\ i\delta m^{+}_{2,z}\end{pmatrix} = P\begin{pmatrix}\delta m^{+}_{1,\phi}\\ \delta m^{+}_{2,\phi}\\ i\delta m^{+}_{1,z}\\ i\delta m^{+}_{2,z}\end{pmatrix}. \tag{14}$$

The 4×4 matrix P is partitioned and antidiagonal. By defining $w \equiv p[\cos2\phi_1 + \cos2\phi_2 + 2\cos(\phi_1 - \phi_2)]$, the nonzero components of P are $P_{1,4} = P_{2,3} = 1 - w$, $P_{1,3} = P_{2,4} = 1 - w + k$, $P_{3,1} = 1 - w\cos2\phi_1 + 2p[\sin(\phi_2 - \phi_1) - \sin2\phi_1]^2 \equiv r$, $P_{4,2} = 1 - w\cos2\phi_2 + 2p[\sin(\phi_2 - \phi_1) + \sin2\phi_2]^2 \equiv t$, and $P_{3,2} = P_{4,1} = \cos(\phi_1 + \phi_2) - w\cos(\phi_1 - \phi_2) + 2p[\sin(\phi_2 - \phi_1) + \sin2\phi_2][\sin(\phi_2 - \phi_1) - \sin2\phi_1] \equiv s$. Suppose P is diagonalized with the form $P\cdot S = S\cdot\mathrm{diag}\{\Omega_1, \Omega_2, \Omega_3, \Omega_4\}$, where Ω_k and $S_{*,k}$ are the eigenvalue (normalized resonance frequency) and the corresponding eigenvector, respectively. Therefore, the spin wave vector for Ω_k is $\delta\mathbf{m}^{+}_1 + \delta\mathbf{m}^{+}_2 \propto (S_{1,k}\mathbf{e}^{1}_{\phi} - iS_{3,k}\mathbf{e}_z) + (S_{2,k}\mathbf{e}^{2}_{\phi} - iS_{4,k}\mathbf{e}_z)$. If $S_{3,k}/S_{1,k}$ is real, $\delta\mathbf{m}^{+}_1$ is elliptically polarized. We then define $S_{3,k}/S_{1,k}$ as the corresponding ellipticity with positive (negative) value indicating right-handed (left-handed) polarity. The same convention applies to $\delta\mathbf{m}^{+}_2$.

For the SF phase ($\phi_1 = \phi_2$), Eq. (8) gives $\cos\phi_1 = -(\sqrt[3]{Y_+} + \sqrt[3]{Y_-})/(24p)$ with $Y_\pm = 96p[-9ph \pm \sqrt{3(27p^2h^2 + 4p)}]$. Then the secular equation, $\det|P - I_{4\times4}\Omega| = 0$, provides $\Omega_1 = -\Omega_2 = \sqrt{k\sin\phi_1\tan\phi_1(3h - 4\cos\phi_1)}$ and

$\Omega_3 = -\Omega_4 = \sqrt{(4\cos\phi_1 - h)[(k+4)\cos\phi_1 - h]}$. When $p < 1/4$, $\Omega_{1\sim4}$ always exist for $h \in (0, h^{\mathrm{FM}})$ and the matrix S reads

$$S = \begin{bmatrix} 1 & 1 & 1 & 1 \\ -1 & -1 & 1 & 1 \\ u & -u & v & -v \\ -u & u & v & -v \end{bmatrix}, \tag{15}$$

with $u \equiv \Omega_1/k > 0$ and $v \equiv \Omega_3/|4 + k - h/\cos\phi_1| > 0$. For the Ω_1 branch, $\delta\mathbf{m}_1^+ \propto \mathbf{e}_\phi^1 - \mathrm{i}u\mathbf{e}_z$ and $\delta\mathbf{m}_2^+ \propto -\mathbf{e}_\phi^2 + \mathrm{i}u\mathbf{e}_z$ are both right-handed polarized, bearing the same ellipticity u when, respectively, facing $+\mathbf{e}_\mathbf{m}^1$ and $+\mathbf{e}_\mathbf{m}^2$. Meantime, they bear a fixed π difference in their phases. For the Ω_2 branch, $\delta\mathbf{m}_{1,2}^+$ become left-handed polarized while the absolute value of the ellipticity and phase difference are unchanged. For the Ω_3 (Ω_4) branch, both $\delta\mathbf{m}_1^+$ and $\delta\mathbf{m}_2^+$ are right-handed (left-handed) with the same ellipticity v ($-v$) and zero phase difference. For all branches, $|\delta\mathbf{m}_1^+|^2 = |\delta\mathbf{m}_2^+|^2$ always holds, implying that the spin waves in the SF phase have the same weight on the two sublattices in each layer. When $p > 1/4$, $\Omega_{1,2}$ still persist for $h \in (0, h^{\mathrm{FM}})$ but $\Omega_{3,4}$ disappear when h falls into $(h_{\min}, h_c)$ with $h_c \equiv \frac{k+4}{2}\sqrt{\frac{k+2}{2p}} > h_{\max}$. Correspondingly, the matrix S becomes

$$S = \begin{cases} \begin{bmatrix} 1 & 1 & 1 & 1 \\ -1 & -1 & 1 & 1 \\ u & -u & v & -v \\ -u & u & v & -v \end{bmatrix}, & h \in (0, h_{\min}] \\ \begin{bmatrix} 1 & 1 & 1 & 1 \\ -1 & -1 & 1 & 1 \\ u & -u & -v & v \\ -u & u & -v & v \end{bmatrix}, & h \in \left[h_c, h^{\mathrm{FM}}\right). \end{cases} \tag{16}$$

For $h \in [h_c, h^{\mathrm{FM}})$, the $\Omega_{3,4}$ branches (if exist) exchange the eigenvectors while leaving the rest unchanged.

Then we turn to the MRS phase ($|\phi_1| < \phi_2 < \pi - |\phi_1|$) which only exists in $[h_{\min}, h_{\max}]$ when $p > 1/4$. Now $w \equiv 1$, thus $P_{1,4} = P_{2,3} = 0$, $P_{1,3} = P_{2,4} = k$, $t > r > 0$, and $rt > s^2$. The eigenfrequencies become $\Omega_1' = -\Omega_2' = \sqrt{(k/2)[(t+r) + \sqrt{(t-r)^2 + 4s^2}]}$ and $\Omega_3' = -\Omega_4' = \sqrt{(k/2)[(t+r) - \sqrt{(t-r)^2 + 4s^2}]}$, which always exist for $h \in [h_{\min}, h_{\max}]$. The corresponding eigenvector matrix reads

$$S' = \begin{bmatrix} 1 & 1 & 1 & 1 \\ \frac{1}{\rho} & \frac{1}{\rho} & -\rho & -\rho \\ u' & -u' & v' & -v' \\ \frac{u'}{\rho} & -\frac{u'}{\rho} & -\rho v' & \rho v' \end{bmatrix}, \tag{17}$$

with $u' \equiv \Omega_1'/k$, $v' \equiv \Omega_3'/k$, and $\rho \equiv [\sqrt{(t-r)^2 + 4s^2} - (t-r)]/(2s)$. For positive (negative) eigenfrequencies $\Omega_{1,3}'$ ($\Omega_{2,4}'$), the corresponding spin waves are right-handed (left-handed). For $\Omega_{1,2}'$ ($\Omega_{3,4}'$) branches, the ellipticity of spin waves is $\pm u'$ ($\pm v'$), while $|\delta\mathbf{m}_1^+|^2/|\delta\mathbf{m}_2^+|^2$ is ρ^2 ($1/\rho^2$). In particular, when $h \to h_s = \sqrt{\frac{4}{3p} - \frac{2}{3}(\sqrt[3]{Y_+} + \sqrt[3]{Y_-})}$ with $Y_\pm = p^{-3} - 72p^{-2} \pm 3p^{-2}\sqrt{6(94 - 4p - 3p^{-1})}$, $s \to 0$. Then $\rho \approx s/(t-r) \to 0$, leading to the dominant $\delta\mathbf{m}_2^+$ ($\delta\mathbf{m}_1^+$) spin-wave components for $\Omega_{1,2}'$ ($\Omega_{3,4}'$) branches. At last, the phase difference between $\delta\mathbf{m}_{1,2}^+$ depends on h. For $h_{\min} < h < h_s$, $\rho < 0$, hence the phase difference is π for $\Omega_{1,2}'$ and 0 for $\Omega_{3,4}'$, respectively. While for $h_s < h < h_{\max}$, ρ becomes positive and the phase difference changes to 0 (π) for $\Omega_{1,2}'$ ($\Omega_{3,4}'$).

3. *Subspace with odd parity under* $\mathbb{C}_{2x}$

The matrix-form spin-wave equation for odd parity reads

$$\Omega \begin{pmatrix} \delta m_{1,\phi}^- \\ \delta m_{2,\phi}^- \\ \mathrm{i}\delta m_{1,z}^- \\ \mathrm{i}\delta m_{2,z}^- \end{pmatrix} = Q \begin{pmatrix} \delta m_{1,\phi}^- \\ \delta m_{2,\phi}^- \\ \mathrm{i}\delta m_{1,z}^- \\ \mathrm{i}\delta m_{2,z}^- \end{pmatrix}. \tag{18}$$

The 4×4 matrix Q is also completely antidiagonal, with the nonzero components $Q_{1,3} = Q_{2,4} = 1 + k + w$, $Q_{1,4} = Q_{2,3} = 1 + w$, $Q_{3,1} = 1 + w\cos 2\phi_1 \equiv \tilde{r}$, $Q_{4,2} = 1 + w\cos 2\phi_2 \equiv \tilde{t}$, and $Q_{3,2} = Q_{4,1} = \cos(\phi_1 + \phi_2) + w\cos(\phi_1 - \phi_2) \equiv \tilde{s}$. It can be further diagonalized as $Q \cdot \tilde{S} = \tilde{S} \cdot \mathrm{diag}\{\tilde{\Omega}_1, \tilde{\Omega}_2, \tilde{\Omega}_3, \tilde{\Omega}_4\}$.

For the SF phase, $\tilde{\Omega}_1 = -\tilde{\Omega}_2 = \sqrt{k\sin\phi_1\tan\phi_1(4\cos\phi_1 - h)}$, $\tilde{\Omega}_3 = -\tilde{\Omega}_4 = \sqrt{h(k\cos\phi_1 + h)}$. When $p < 1/4$, they always exist when $h \in (0, h^{\mathrm{FM}})$. Then $\tilde{S}$ reads

$$\tilde{S} = \begin{bmatrix} 1 & 1 & 1 & 1 \\ -1 & -1 & 1 & 1 \\ \tilde{u} & -\tilde{u} & \tilde{v} & -\tilde{v} \\ -\tilde{u} & \tilde{u} & \tilde{v} & -\tilde{v} \end{bmatrix}, \tag{19}$$

with $\tilde{u} \equiv \tilde{\Omega}_1/k > 0$ and $\tilde{v} \equiv \tilde{\Omega}_3/(k + h/\cos\phi_1) > 0$. Again for all positive (negative) eigenfrequencies $\tilde{\Omega}_{1,3}$ ($\tilde{\Omega}_{2,4}$), the corresponding spin waves are right-handed (left-handed) while the phase difference between $\delta\mathbf{m}_{1,2}^-$ for $\tilde{\Omega}_{1,2}$ ($\tilde{\Omega}_{3,4}$) is π (0). When p is larger than $1/4$, $\tilde{\Omega}_{1,2}$ (and the corresponding eigenvectors) only exist for $h \in (0, h_{\min}]$, while $\tilde{\Omega}_{3,4}$ persist.

For the MRS phase, $w \equiv 1$ thus $Q_{1,4} = Q_{2,3} = 2$ and $Q_{1,3} = Q_{2,4} = 2 + k$. Now $\tilde{r} > \tilde{t} > 0$ and $\tilde{r}\tilde{t} = \tilde{s}^2$. In particular, $\tilde{s} > 0$ for $p < 2$, which is reasonable for real all-antiferromagnetic junctions. The eigenfrequencies then become $\tilde{\Omega}_1' = \tilde{\Omega}_2' = 0$ and $\tilde{\Omega}_3' = -\tilde{\Omega}_4' = \sqrt{(k+2)(\tilde{r} + \tilde{t}) + 4\tilde{s}}$, which always exist for $h \in [h_{\min}, h_{\max}]$. Correspondingly, the eigenvector matrix is

$$\tilde{S}' = \begin{bmatrix} 1 & 1 & 1 & 1 \\ -\tilde{\rho} & -\tilde{\rho} & \tilde{\lambda} & \tilde{\lambda} \\ 0 & 0 & \tilde{u}' & -\tilde{u}' \\ 0 & 0 & \tilde{\lambda}\tilde{v}' & -\tilde{\lambda}\tilde{v}' \end{bmatrix}, \tag{20}$$

with $\tilde{\rho} \equiv [(2+k)\tilde{r} + 2\tilde{s}]/[(2+k)\tilde{s} + 2\tilde{t}]$, $\tilde{\lambda} \equiv [(2+k)\tilde{t} + 2\tilde{s}]/[(2+k)\tilde{s} + 2\tilde{t}]$, $\tilde{u}' = \tilde{\Omega}_3'\tilde{s}/[(2+k)\tilde{s} + 2\tilde{t}]$, and $\tilde{v}' = \tilde{\Omega}_3'\tilde{t}/[(2+k)\tilde{t} + 2\tilde{s}]$. For $\tilde{\Omega}_{1,2}' = 0$, $\delta\mathbf{m}_1^-$ ($\delta\mathbf{m}_2^-$) only has a time-independent component along $\mathbf{e}_\phi^1$ ($\mathbf{e}_\phi^2$) in the xy plane. On the other hand, for $\tilde{\Omega}_3'$, the spin-wave components $\delta\mathbf{m}_1^-$ and $\delta\mathbf{m}_2^-$ are both right-handed polarized with synchronous phases and different ellipticity ($\tilde{u}'$ and $\tilde{v}'$, respectively). A similar situation holds for $\tilde{\Omega}_4'$; the only difference is that the polarization reverses. At last, for $\tilde{\Omega}_{3,4}'$ branches, $|\delta\mathbf{m}_1^+|^2/|\delta\mathbf{m}_2^+|^2 = \tilde{u}'/(\tilde{\lambda}^2\tilde{v}')$, implying that the spin waves in

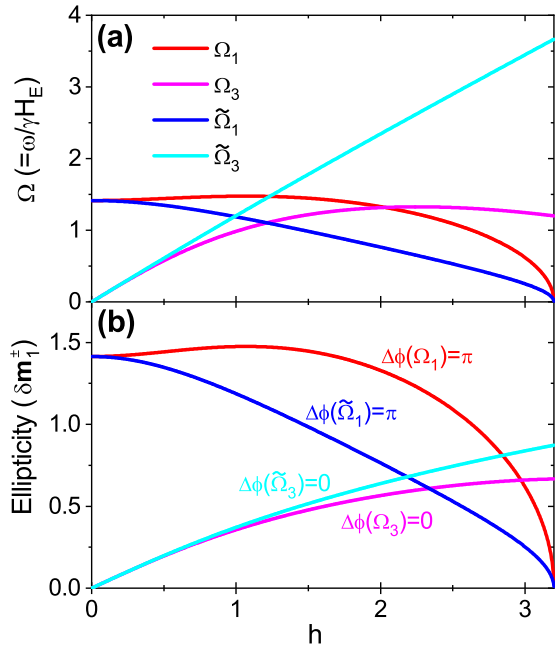

FIG. 4. Eigenfrequencies, ellipticities, and phase differences of spin-wave components $\delta\mathbf{m}^{\pm}_{1,2}$ in symmetrical all-antiferromagnetic junctions with $k = 1$ and $p = 0.15$ under in-plane dc fields $h \in (0, h^{\rm FM})$. The equilibrium magnetization layout falls into the SF phase. (a) Four positive eigenfrequencies: Ω_1 (red), Ω_3 (magenta), $\tilde{\Omega}_1$ (blue) and $\tilde{\Omega}_3$ (cyan). (b) Ellipticities of $\delta\mathbf{m}^{+}_1$ for $\Omega_{1,3}$ and $\delta\mathbf{m}^{-}_1$ for $\tilde{\Omega}_{1,3}$, which are identical to those of $\delta\mathbf{m}^{\pm}_2$. The corresponding phase differences between $\delta\mathbf{m}^{\pm}_{1,2}$ for all four branches are indicated.

the MRS phase with odd parity have different weights on the two sublattices in each layer.

4. Numerical examples and asymptotics

To be more intuitive, the eigenfrequencies and corresponding spin-wave features with $k = 1$ and two typical values of p are calculated. In Fig. 4, $p = 0.15$, hence the SF phase is the only choice for the ground state. The four positive eigenfrequency branches, $\Omega_{1,3}$ with even parity and $\tilde{\Omega}_{1,3}$ with odd parity, are plotted in Fig. 4(a). First, Ω_1 (red) and $\tilde{\Omega}_1$ (blue) both start from $\sqrt{2k}$ at $h = 0$ but have different concavity: For $h = \iota \ll 1$,

$$\Omega_1 \approx \sqrt{2k}\left[1 + \frac{1}{2}\left(p - \frac{1}{4}\right)\iota^2\right],$$
$$\tilde{\Omega}_1 \approx \sqrt{2k}\left[1 - \frac{1}{2}\left(p + \frac{1}{4}\right)\iota^2\right]. \tag{21}$$

Then they converge to 0 at $h = h^{\rm FM}$ as

$$\Omega_1 \approx 2\sqrt{k(1+12p)f(p)}\sqrt{\iota},$$
$$\tilde{\Omega}_1 \approx 2\sqrt{k(1-4p)f(p)}\sqrt{\iota}, \tag{22}$$

with $\iota \equiv h^{\rm FM} - h$ and $f(p) \equiv [\sqrt[3]{\sqrt{(h^{\rm FM})^2 + \frac{4}{27p}} - h^{\rm FM}} + \sqrt[3]{2p}]/[3\sqrt[3]{2p}\sqrt{(h^{\rm FM})^2 + \frac{4}{27p}}\,]$. As for Ω_3 (magenta) and $\tilde{\Omega}_3$ (cyan), around $h = 0$ they both linearly increase with the same slope $\sqrt{(k+2)/2}$ and have no other zero points. In particular, $\tilde{\Omega}_3$ is approximately linear with h in the full range of $h \in (0, h^{\rm FM})$. As a consequence, we have a total of four accidental crossings (two interparity and two intraparity) in the resonance spectrum. In Fig. 4(b), the corresponding ellipticities of $\delta\mathbf{m}^{\pm}_1$ for the four branches (+ for $\Omega_{1,3}$, – for $\tilde{\Omega}_{1,3}$) from Fig. 4(a) are plotted. Note that for $p < 1/4$, ellipticities of $\delta\mathbf{m}^{\pm}_2$ coincide with those of $\delta\mathbf{m}^{\pm}_1$ for each branch so we have not provided them. For Ω_1 and $\tilde{\Omega}_1$, ellipticities of $\delta\mathbf{m}^{\pm}_1$ decreases from $\sqrt{2/k}$ (at $h = 0$) to 0 (at $h^{\rm FM}$), implying a transition from circular to linear (in the xy plane) polarization of $\delta\mathbf{m}^{\pm}_1$ as h increases. Accordingly, the phase difference between $\delta\mathbf{m}^{\pm}_1$ and $\delta\mathbf{m}^{\pm}_2$ is always π, as indicated in Fig. 4(b). Alternatively, for Ω_3 and $\tilde{\Omega}_3$, ellipticities of $\delta\mathbf{m}^{\pm}_1$ increases from 0 (at $h = 0$) to, respectively, $\sqrt{(1-4p)/(1-4p+k/2)}$ and $\sqrt{(1+4p)/(1+4p+k/2)}$ (at $h^{\rm FM}$), indicating a linear to circular polarization transition of spin waves while the phase difference between $\delta\mathbf{m}^{\pm}_1$ and $\delta\mathbf{m}^{\pm}_2$ changes to 0. At last, the spin-wave intensity ratio, $|\delta\mathbf{m}^{\pm}_1|^2/|\delta\mathbf{m}^{\pm}_2|^2$, always equals 1 for all frequency branches, implying an equal weighting of spin waves in the SF phase.

In Fig. 5, p increases to 0.45, hence either the SF or MRS phase can be the ground state, which has been indicated, respectively, by white or shaded areas. Based on them, $\Omega_1 \cup \Omega_1'$, $\Omega_3 \cup \Omega_3'$, $\tilde{\Omega}_1 \cup \tilde{\Omega}_1'$, and $\tilde{\Omega}_3 \cup \tilde{\Omega}_3'$ are provided in Fig. 5(a). Here branches without (with) a prime are in the SF (MRS) phase. Still, two interparity (red-cyan, blue-magenta) and two intraparity (red-magenta, blue-cyan) crossings exist (blue-magenta crossing occurs around $h = 2.075$ and is not very clear in this dimension). The asymptotic behaviors of these four branches around $h = 0$ are the same as Eq. (21), however, due to the emergence of the MRS phase in $[h_{\rm min}, h_{\rm max}]$ with $h_{\rm min} = 2.9814$ and $h_{\rm max} = 3.5277$, several interesting changes occur. Recalling that at $h = h_{\rm min}$ ($h_{\rm max}$) the equilibrium system undergoes a second-order (first-order) PT, hence both $\Omega_1 \cup \Omega_1'$ and $\tilde{\Omega}_3 \cup \tilde{\Omega}_3'$ are continuous (discontinuous) at $h = h_{\rm min}$ ($h_{\rm max}$). Except for this, Ω_1 and $\tilde{\Omega}_3$ do not change much compared with the counterparts under $p = 0.15$. The other two, however, have changed dramatically. For $\Omega_3 \cup \Omega_3'$ (magenta), three extra zero points ($h_{\rm min}$, $h_{\rm max}$ and $h_c = 4.5644$) emerge, with the following asymptotic behaviors:

$$\begin{cases} \iota = \begin{cases} h_{\rm min} - h:\ \Omega_3 = \sqrt{\frac{1}{4}kh_{\rm min}}\sqrt{\iota} \\ h - h_{\rm min}:\ \Omega_3' = \sqrt{\frac{22p-1}{16p-4}kh_{\rm min}}\sqrt{\iota} \end{cases} \\ \iota = h_{\rm max} - h:\ \Omega_3' = \sqrt{\frac{4p}{8p+3}kh_{\rm max}}\sqrt{\iota} \\ \iota = h - h_c:\ \Omega_3 = 2\sqrt{h_c[1+(k+4)g(p)]}\sqrt{\iota}, \end{cases} \tag{23}$$

where $0 < \iota \ll 1$ and $g(p) \equiv [\sqrt[3]{\sqrt{(h_c)^2 + \frac{4}{27p}} - h_c} + \frac{1}{2}\sqrt{\frac{k+2}{2p}}\sqrt[3]{2p}]/[3\sqrt[3]{2p}\sqrt{(h_c)^2 + \frac{4}{27p}}\,]$, while for $\tilde{\Omega}_1 \cup \tilde{\Omega}_1'$ (blue), the part in the SF phase shrinks to $(0, h_{\rm min})$ with the following asymptotic behavior on the left of $h_{\rm min}$:

$$\tilde{\Omega}_1 \approx \sqrt{k\frac{16 - h_{\rm min}^2}{4h_{\rm min}}}\sqrt{\iota}, \quad \iota = h_{\rm min} - h. \tag{24}$$

In addition, the zero flat $\tilde{\Omega}_1'$ spectrum in the MRS phase indicates a time-independent magnetization deviation in the

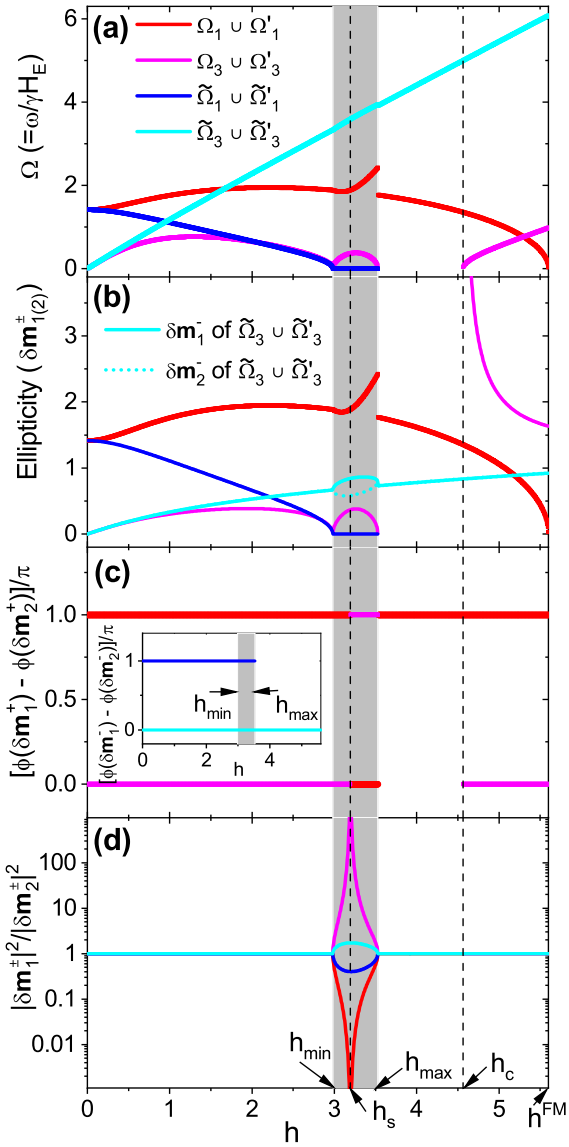

FIG. 5. Eigenfrequencies, ellipticities, phase differences and weight ratios of spin-wave components in symmetrical all-antiferromagnetic junctions with $k = 1$ and $p = 0.45$ under in-plane dc fields with $h \in (0, h^{\mathrm{FM}})$. The equilibrium magnetization layout can be either SF (white) or MRS (shaded) phase. (a) Four positive eigenfrequencies Ω_1 (red), Ω_3 (magenta), $\tilde{\Omega}_1$ (blue), and $\tilde{\Omega}_3$ (cyan). (b) Solid (dashed) curves are the ellipticities of $\delta\mathbf{m}_1^{\pm}$ ($\delta\mathbf{m}_2^{\pm}$) for all four branches. (c) Phase differences between $\delta\mathbf{m}_{1,2}^{+}$ for $\Omega_{1,3}$ branches. Those for $\tilde{\Omega}_{1,3}$ are provided in the inset. (d) Intensity ratio of the spin-wave component on group 1 over that on group 2. In SF phase (white area) the data from all four branches (if exist) coincide, while in MRS phase (shaded area) they split.

xy plane from the equilibrium layout. In 2021, Yuan and Duine revealed that the resonance frequency ω follows a universal power law $\omega \propto |H - H_c|^q$, where H_c is the critical field at which the resonance frequency is zero [47]. When the magnet preserves rotational symmetry around the external field $\mathbf{H}$, $q = 1$, otherwise, $q = 1/2$. All of our asymptotic results on eigenfrequencies [Eqs. (22) to (24)] confirm their claims. In addition, they asserted that the zero frequency is often accompanied by a reorientation transition in the magnetization. For the case in which $q = 1/2$, this transition is described by a Landau theory for second-order PTs. In our symmetric all-antiferromagnetic junctions, the PT at $h = h_{\mathrm{min}}$ (SF $\leftrightarrow$MRS) is applicable to this conclusion, however, the one at $h = h_{\mathrm{max}}$ (MRS $\leftrightarrow$ SF) breaks this rule. At last, interparity and intraparity crossings still coexist.

In Fig. 5(b), ellipticities of $\delta\mathbf{m}_{1,2}^{\pm}$ are provided. For the entire region of $h \in (0, h^{\mathrm{FM}})$, ellipticities of $\delta\mathbf{m}_2$ coincide with those of $\delta\mathbf{m}_1$ for $\Omega_1 \cup \Omega'_1$, $\Omega_3 \cup \Omega'_3$, and $\tilde{\Omega}_1 \cup \tilde{\Omega}'_1$, so we only provide the latter. As for $\tilde{\Omega}_3 \cup \tilde{\Omega}'_3$, inconsistency occurs in the MRS phase, which has been indicated by the departure of solid and dotted cyan curves. On one hand, the two branches with odd parity ($\tilde{\Omega}_1 \cup \tilde{\Omega}'_1$ and $\tilde{\Omega}_3 \cup \tilde{\Omega}'_3$) are relatively simple. Ellipticity of $\delta\mathbf{m}_{1,2}^{-}$ from the $\tilde{\Omega}_1 \cup \tilde{\Omega}'_1$ ($\tilde{\Omega}_3 \cup \tilde{\Omega}'_3$) branch decreases (increases) from $\sqrt{2/k}$ (0) at $h = 0$ to 0 ($\sqrt{(1+4p)/(1+4p+k/2)}$) at $h = h_{\mathrm{min}}$ (h_{max}), indicating a gradual evolution from circular (linear) to linear (circular) polarization of $\delta\mathbf{m}_{1,2}^{-}$ as h increases, while the phase difference between $\delta\mathbf{m}_{1,2}^{-}$ is fixed as π (0) whenever the eigenfrequency exists, as shown in the inset of Fig. 5(c). The intensity ratio, $|\delta\mathbf{m}_1^{-}|^2/|\delta\mathbf{m}_2^{-}|^2$, keeps 1 in the SF phase for both $\tilde{\Omega}_1 \cup \tilde{\Omega}'_1$ and $\tilde{\Omega}_3 \cup \tilde{\Omega}'_3$ branches, and separates in MRS phase [see Fig. 5(d)]. Clearly, in the $\tilde{\Omega}'_1$ ($\tilde{\Omega}'_3$) branch, $\delta\mathbf{m}_2^{-}$ ($\delta\mathbf{m}_1^{-}$) dominates. On the other hand, the two branches with even parity ($\Omega_1 \cup \Omega'_1$ and $\Omega_3 \cup \Omega'_3$) are more complex. The emergence of the MRS phase separates the ellipticity of the $\Omega_3 \cup \Omega'_3$ branch into four parts and the corresponding three dividing points are h_{min}, h_{max}, and h_c, as shown in Fig. 5(b). At the former two (the last one), $\delta\mathbf{m}_{1,2}^{+}$ become linearly polarized in the xy plane (z axis). As for the $\Omega_1 \cup \Omega'_1$ branch, the ellipticity becomes concave in the MRS phase rather than convex in the SF phase, leading to a discontinuity at h_{max}. Greater interest resides in the intensity ratio in the MRS phase. For the $\Omega_1 \cup \Omega'_1$ ($\Omega_3 \cup \Omega'_3$) branch, spin waves are concentrated on $\delta\mathbf{m}_2^{+}$ ($\delta\mathbf{m}_1^{+}$), as depicted in Fig. 5(d). In particular, at $h_s = 3.1955$ only $\delta\mathbf{m}_2^{+}$ ($\delta\mathbf{m}_1^{+}$) exists. When h exceeds h_s, $\delta\mathbf{m}_1^{+}$ ($\delta\mathbf{m}_2^{+}$) components reappear, however, the phase difference between $\delta\mathbf{m}_{1,2}^{+}$ exchanges ($0 \leftrightarrow \pi$) compared with the case where $h < h_s$ [see Fig. 5(c)]. This reminds us of the level-reversal behavior in topological insulators after the bulk gap closes and then reopens.

C. Oblique-dc-field case

Under in-plane dc fields, the absence of entanglement between subspaces with opposite parity under $\mathbb{C}_{2x}$ leads to the complete decoupling in the dynamic equations of $\delta\mathbf{m}_{1,2}^{+}$ and $\delta\mathbf{m}_{1,2}^{-}$ [see Eq. (13)]. This further results in the accidental crossings between frequency branches with opposite parity in resonance spectrums, implying the absence of magnon-magnon couplings in this system. To induce it, a reasonable attempt is exerting an oblique dc field with $0 < \psi < \pi/2$. Systematical investigations on the impact of oblique dc fields on coherent magnonics constitute the main content of this subsection.

1. Emergence of couplings

For the SF phase, $\mathbf{e}_{x'} \equiv \mathbf{e}_{x''} \neq \mathbf{e}_x$, $\mathbf{e}_{y'} \equiv \mathbf{e}_{y''} = \mathbf{e}_y$, and $\mathbf{e}_{z'} \equiv \mathbf{e}_{z''} \neq \mathbf{e}_z$, thus $\mathbb{C}_{2x'} = \mathbb{C}_{2x''} \equiv \mathbb{C} \neq \mathbb{C}_{2x}$. In the skewed local

coordinate systems $(\mathbf{e}_{\mathbf{m}}^{1(2)} \equiv \mathbf{m}_{A,1(2)}^{\rm eq}, \mathbf{e}_{\phi}^{1(2)} \equiv \mathbf{e}_{z'} \times \mathbf{e}_{\mathbf{m}}^{1(2)}, \mathbf{e}_{z'})$, similarly we decompose $\delta\mathbf{m}_{1(2)}^{\pm}$ as $\delta\mathbf{m}_{1(2)}^{\pm} = \delta m_{1(2),\phi}^{\pm}\mathbf{e}_{\phi}^{1(2)} + \delta m_{1(2),z'}^{\pm}\mathbf{e}_{z'}$, which are the spin-wave components with even (+) and odd (–) parities under $\mathbb{C}$. Hence, Eq. (12) becomes

$$\begin{aligned}
\mathrm{i}\Omega\delta\mathbf{m}_{1(2)}^{+} = \mathbf{m}_{A,1(2)}^{\rm eq} \times \Big\{ & (\delta\mathbf{m}_{1}^{+} + \delta\mathbf{m}_{2}^{+}) \\
& + 2p\big[\mathbf{m}_{B}^{\rm eq} \cdot (\delta\mathbf{m}_{1}^{+} + \delta\mathbf{m}_{2}^{+})\big]\mathbf{m}_{B}^{\rm eq} \\
& + p\big(\mathbf{m}_{A}^{\rm eq} \cdot \mathbf{m}_{B}^{\rm eq}\big)\mathbb{C}(\delta\mathbf{m}_{1}^{+} + \delta\mathbf{m}_{2}^{+}) \\
& + \frac{k}{2}[\mathbf{e}_z(\mathbf{e}_z\cdot) + \mathbb{C}\mathbf{e}_z(\mathbb{C}\mathbf{e}_z\cdot)]\delta\mathbf{m}_{1(2)}^{+} \\
& + \frac{k}{2}[\mathbf{e}_z(\mathbf{e}_z\cdot) - \mathbb{C}\mathbf{e}_z(\mathbb{C}\mathbf{e}_z\cdot)]\delta\mathbf{m}_{1(2)}^{-} \Big\}, \\
\mathrm{i}\Omega\delta\mathbf{m}_{1(2)}^{-} = \mathbf{m}_{A,1(2)}^{\rm eq} \times \Big\{ & (\delta\mathbf{m}_{1}^{-} + \delta\mathbf{m}_{2}^{-}) \\
& - p\big(\mathbf{m}_{A}^{\rm eq} \cdot \mathbf{m}_{B}^{\rm eq}\big)\mathbb{C}(\delta\mathbf{m}_{1}^{-} + \delta\mathbf{m}_{2}^{-}) \\
& + \frac{k}{2}[\mathbf{e}_z(\mathbf{e}_z\cdot) + \mathbb{C}\mathbf{e}_z(\mathbb{C}\mathbf{e}_z\cdot)]\delta\mathbf{m}_{1(2)}^{-} \\
& + \frac{k}{2}[\mathbf{e}_z(\mathbf{e}_z\cdot) - \mathbb{C}\mathbf{e}_z(\mathbb{C}\mathbf{e}_z\cdot)]\delta\mathbf{m}_{1(2)}^{+} \Big\}. \qquad (25)
\end{aligned}$$

Clearly, $\mathbb{C}\mathbf{e}_z \neq -\mathbf{e}_z$ (since $\mathbf{e}_{x'} \neq \mathbf{e}_x$), leading to the couplings between subspaces with opposite parity under $\mathbb{C}$ and further the possible anticrossings in resonance spectrum.

To see more clearly, by defining $\Lambda \equiv (\delta m_{1,\phi}^{+}, \delta m_{2,\phi}^{+}, \mathrm{i}\delta m_{1,z'}^{+}, \mathrm{i}\delta m_{2,z'}^{+}, \delta m_{1,\phi}^{-}, \delta m_{2,\phi}^{-}, \mathrm{i}\delta m_{1,z'}^{-}, \mathrm{i}\delta m_{2,z'}^{-})^{\rm T}$, the above vectorial equation set becomes

$$P_{\rm SF}\Lambda = \Omega\Lambda, \quad P_{\rm SF} = \begin{bmatrix} \Theta & \Gamma \\ \Gamma & \Phi \end{bmatrix}, \qquad (26)$$

with

$$\Theta = \begin{bmatrix} 0 & 0 & a_1 + k\cos^2\chi & a_1 \\ 0 & 0 & a_1 & a_1 + k\cos^2\chi \\ b_1 & b_2 & 0 & 0 \\ b_2 & b_1 & 0 & 0 \end{bmatrix},$$

$$\Phi = \begin{bmatrix} 0 & 0 & a_2 + k\cos^2\chi & a_2 \\ 0 & 0 & a_2 & a_2 + k\cos^2\chi \\ c_1 & c_2 & 0 & 0 \\ c_2 & c_1 & 0 & 0 \end{bmatrix},$$

$$\Gamma = \mathrm{i} \times \mathrm{diag}\{-d, d, d, -d\}, \qquad (27)$$

where the definitions of $a_{1,2}$, $b_{1,2}$, $c_{1,2}$, and d are provided in Eq. (A2). The nonzero ψ results in finite d, hence the nonvanishing coupling matrix Γ. In principle, by numerically diagonalizing $P_{\rm SF}$, the eigenfrequencies, the hybridization of even and odd subspaces, the ellipticities, and phase difference between spin-wave components can be obtained. Specifically, the secular equation for resonance frequency can be reduced to a standard quartic algebraic equation of Ω^2: $(\Omega^2)^4 + J_3(\Omega^2)^3 + J_2(\Omega^2)^2 + J_1(\Omega^2) + J_0 = 0$. The explicit expressions of J_i (functions of χ and ϵ) have been provided in Appendix A due to their lengthy forms. By solving it, the eigenfrequencies in the SF phase can be obtained and cross-verified with data from direct diagonalization. In addition, the pure-imaginary coupling matrix Γ (as long as $\psi > 0$) has two important consequences on the eigenvectors: (i) Nonvanishing hybridization between subspaces with even and odd parities under $\mathbb{C}$ persists. (ii) There is always a phase difference of $\pm\frac{\pi}{2}$ between components in subspaces with even and odd parities.

For the MRS phase, $\mathbf{e}_{x'} \neq \mathbf{e}_{x''}$ then $\mathbb{C}_{2x'}\mathbf{m}_{A,2}^{\rm eq} \neq \mathbf{m}_{B,2}^{\rm eq}$ and $\mathbb{C}_{2x''}\mathbf{m}_{A,1}^{\rm eq} \neq \mathbf{m}_{B,1}^{\rm eq}$. The only possible parity operator is the mirror reflection $\mathbb{M}_{xz}$. We then construct $\mathbf{l}_{1(2)}^{\pm} \equiv \delta\mathbf{m}_{A,1(2)} \pm \mathbb{M}_{xz}\delta\mathbf{m}_{B,1(2)}$ as the spin-wave components with even (+) and odd (–) parities under $\mathbb{M}_{xz}$. Note that $\mathbb{M}_{xz}(\mathbf{U}\cdot\mathbf{V}) = \mathbb{M}_{xz}\mathbf{U}\cdot\mathbb{M}_{xz}\mathbf{V}$ and $\mathbb{M}_{xz}(\mathbf{U}\times\mathbf{V}) = -\mathbb{M}_{xz}\mathbf{U}\times\mathbb{M}_{xz}\mathbf{V}$, where $\mathbf{U}$ and $\mathbf{V}$ are arbitrary vectors, therefore $\mathbb{M}_{xz}$ does not preserve the polarization of spin waves, which is quite different from the rotation operators $\mathbb{C}_{2x(x',x'')}$. Now Eq. (12) becomes

$$\begin{aligned}
\mathrm{i}\Omega\mathbf{l}_{1(2)}^{+} = \mathbf{m}_{A,1(2)}^{\rm eq} \times \Big\{ & (\mathbf{l}_{1}^{-} + \mathbf{l}_{2}^{-}) + k(\mathbf{l}_{1(2)}^{-}\cdot\mathbf{e}_z)\mathbf{e}_z \\
& - p\big(\mathbf{m}_{A}^{\rm eq}\cdot\mathbf{m}_{B}^{\rm eq}\big)\mathbb{M}_{xz}(\mathbf{l}_{1}^{-} + \mathbf{l}_{2}^{-})\Big\}, \\
\mathrm{i}\Omega\mathbf{l}_{1(2)}^{-} = \mathbf{m}_{A,1(2)}^{\rm eq} \times \Big\{ & (\mathbf{l}_{1}^{+} + \mathbf{l}_{2}^{+}) + k(\mathbf{l}_{1(2)}^{+}\cdot\mathbf{e}_z)\mathbf{e}_z \\
& + p\big(\mathbf{m}_{A}^{\rm eq}\cdot\mathbf{m}_{B}^{\rm eq}\big)\mathbb{M}_{xz}(\mathbf{l}_{1}^{+} + \mathbf{l}_{2}^{+}) \\
& + 2p\big[\mathbf{m}_{B}^{\rm eq}\cdot(\mathbf{l}_{1}^{+} + \mathbf{l}_{2}^{+})\big]\mathbf{m}_{B}^{\rm eq}\Big\}. \qquad (28)
\end{aligned}$$

Recall that the angle between $\mathbf{e}_{x'}$ ($\mathbf{e}_{x''}$) and $\mathbf{e}_x$ is χ (ξ) while the angle between $\mathbf{e}_{x'}$ and $\mathbf{m}_{A,1}^{\rm eq}$ ($\mathbf{e}_{x''}$ and $\mathbf{m}_{A,2}^{\rm eq}$) is ϵ (η). For MRS phase under oblique dc fields, generally $0 < \chi < \xi < \frac{\pi}{2} - \psi$. We then denote the plane expanded by $\mathbf{m}_{A,1}^{\rm eq}$ and $\mathbf{m}_{B,1}^{\rm eq}$ ($\mathbf{m}_{A,2}^{\rm eq}$ and $\mathbf{m}_{B,2}^{\rm eq}$) as the χ−plane (ξ−plane). On each oblique plane, we define the following local coordinate system: (i) χ-plane-based: $(\mathbf{e}_{\mathbf{m}}^{1} \equiv \mathbf{m}_{A,1}^{\rm eq}, \mathbf{e}_{\phi}^{1} \equiv \mathbf{e}_{z'} \times \mathbf{e}_{\mathbf{m}}^{1}, \mathbf{e}_{z'} = -\sin\chi\mathbf{e}_x + \cos\chi\mathbf{e}_z)$ and (ii) ξ-plane-based: $(\mathbf{e}_{\mathbf{m}}^{2} \equiv \mathbf{m}_{A,2}^{\rm eq}, \mathbf{e}_{\phi}^{2} \equiv \mathbf{e}_{z''} \times \mathbf{e}_{\mathbf{m}}^{1}, \mathbf{e}_{z''} = -\sin\xi\mathbf{e}_x + \cos\xi\mathbf{e}_z)$. Then we decompose $\mathbf{l}_{1(2)}^{\pm}$ as $\mathbf{l}_{1}^{\pm} = l_{1,\phi}^{\pm}\mathbf{e}_{\phi}^{1} + l_{1,z'}^{\pm}\mathbf{e}_{z'}$ and $\mathbf{l}_{2}^{\pm} = l_{2,\phi}^{\pm}\mathbf{e}_{\phi}^{2} + l_{2,z''}^{\pm}\mathbf{e}_{z''}$. After defining $\tilde{\Lambda} \equiv (l_{1,\phi}^{+}, l_{2,\phi}^{+}, \mathrm{i}l_{1,z'}^{+}, \mathrm{i}l_{2,z''}^{+}, l_{1,\phi}^{-}, l_{2,\phi}^{-}, \mathrm{i}l_{1,z'}^{-}, \mathrm{i}l_{2,z''}^{-})^{\rm T}$, Eq. (28) is rewritten as

$$P_{\rm MRS}\tilde{\Lambda} = \Omega\tilde{\Lambda}, \quad P_{\rm MRS} = \begin{bmatrix} 0_{4\times4} & \tilde{\Theta} \\ \tilde{\Phi} & 0_{4\times4} \end{bmatrix}, \qquad (29)$$

in which $\tilde{\Theta}$ and $\tilde{\Phi}$ are both 4×4 matrices, with detailed expressions of each element provided in Appendix B. Clearly, entanglements between subspaces with opposite parity under $\mathbb{M}_{xz}$ emerge, thus the crossings (if they exist) in the resonance spectrum become anticrossings. Again, by directly diagonalizing $P_{\rm MRS}$, the eigenfrequencies, eigenvectors, and corresponding features can be obtained. In particular, the secular equation, $|P_{\rm MRS} - \Omega I_{8\times8}| = 0$, is reduced to $|\tilde{\Theta}\tilde{\Phi} - \Omega^2 I_{4\times4}| = 0$, which is also a quartic algebraic equation of Ω^2. However, the detailed expression is too complicated to be explicitly written out. One can numerically solve it to cross verify the data from direct diagonalization.

2. Numerical examples

To have a direct impression on the oblique-field-induced magnon-magnon coupling, we take $\psi = \pi/10$ as an example while leaving other parameters (p and k) the same as in Figs. 4 and 5 (in-plane-dc-field case). Considering the possible anticrossings in the resonance spectrum (thus hybridize the original branches with even and odd parities under rotation

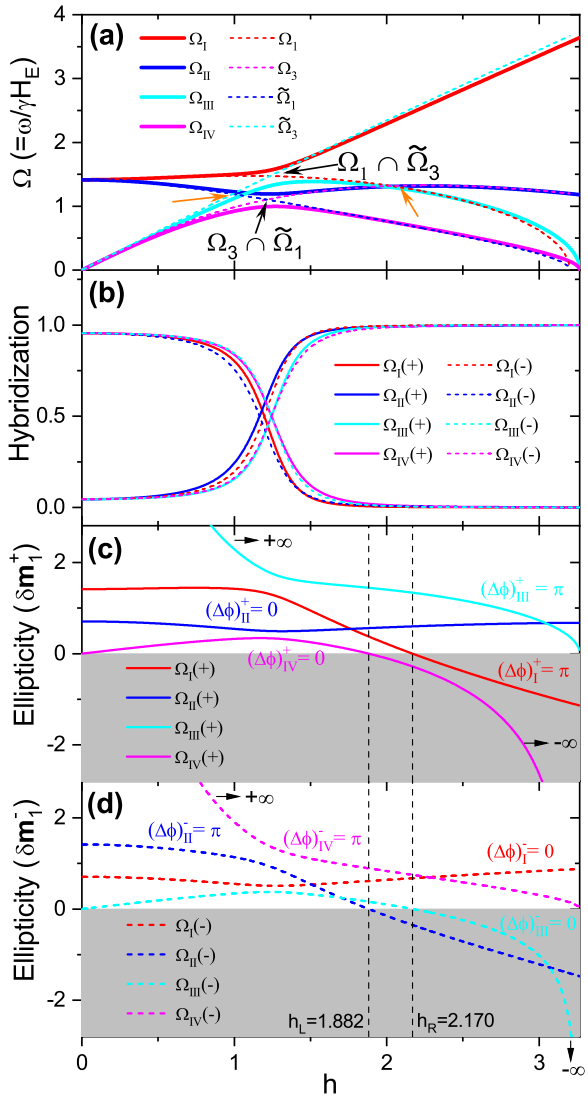

FIG. 6. Eigenfrequencies, hybridizations, ellipticities, and phase differences of spin-wave components $\delta\mathbf{m}^{\pm}_{\mathrm{I},2}$ in symmetrical all-antiferromagnetic junctions with $k = 1$ and $p = 0.15$ under oblique dc fields with $\psi = \pi/10$ and $h \in (0, h^{\mathrm{FM}})$. The equilibrium magnetization layout falls into the SF phase. (a) Four positive eigenfrequencies Ω_{I} (red), Ω_{II} (blue), Ω_{III} (cyan), and Ω_{IV} (magenta). The dashed curves are Ω_1 (red), Ω_3 (magenta), $\tilde{\Omega}_1$ (blue), and $\tilde{\Omega}_3$ (cyan) for in-plane-dc-field cases [see Fig. 4(a)]. Black arrows indicate the interparity crossing points $\Omega_1 \cap \tilde{\Omega}_3$ and $\tilde{\Omega}_1 \cap \Omega_3$ while orange arrows indicate the intraparity ones: $\Omega_1 \cap \Omega_3$ and $\tilde{\Omega}_1 \cap \tilde{\Omega}_3$. (b) Evolution of hybridization between subspaces with even and odd parities for all four eigenfrequencies. Solid (dashed) lines indicate $|\delta\mathbf{m}^{+}_{1}|^2 + |\delta\mathbf{m}^{+}_{2}|^2$ ($|\delta\mathbf{m}^{-}_{1}|^2 + |\delta\mathbf{m}^{-}_{2}|^2$). (c) Ellipticities of $\delta\mathbf{m}^{+}_{1}$ for all four eigenfrequencies, which are identical to those of $\delta\mathbf{m}^{+}_{2}$. The corresponding phase differences between $\delta\mathbf{m}^{+}_{1,2}$ are indicated. (d) Counterparts of (c) for $\delta\mathbf{m}^{-}_{1,2}$.

or mirror reflection operators), in this section we name the four positive eigenfrequency branches as Ω_{I}, Ω_{II}, Ω_{III}, and Ω_{IV} in the order from highest to lowest around $h = 0$.

For $p = 0.15$, only frequency branches in the SF phase exist. In Fig. 6(a), the four positive eigenfrequencies ($\Omega_{\mathrm{I\sim IV}}$) are plotted by solid curves while we repaint the four frequency branches in Fig. 4(a) by dashed curves. The interparity crossing points under in-plane dc fields, $\Omega_1 \cap \tilde{\Omega}_3$ and $\tilde{\Omega}_1 \cap \Omega_3$, are lifted by oblique dc fields and become anticrossings [see black arrows in Fig. 6(a)] while the intraparity ones ($\Omega_1 \cap \Omega_3$ and $\tilde{\Omega}_1 \cap \tilde{\Omega}_3$) persist [orange arrows in Fig. 6(a)]. For each eigenfrequency, its corresponding eigenvector is the superposition of $\delta\mathbf{m}^{\pm}_{1,2}$. The weights in subspaces with even and odd parities are described by $|\delta\mathbf{m}^{+}_{1}|^2 + |\delta\mathbf{m}^{+}_{2}|^2$ and $|\delta\mathbf{m}^{-}_{1}|^2 + |\delta\mathbf{m}^{-}_{2}|^2$, respectively. The variation of these weights as h increases depicts the evolution of subspace hybridization, as shown in Fig. 6(b). Originally, the hybridization is relatively weak when $h \sim 0$ and each eigenvector preserves its main weight similar to those from the in-plane-dc-field case. When h increases, around each anticrossing the eigenvector experiences a strong hybridization and is then almost evenly distributed in the two subspaces. As h is further strengthened, the eigenvector transfers its most weight to the subspace with opposite parity. In addition, the pure-imaginary coupling matrix Γ always results in a $\pi/2$ phase difference between $\delta\mathbf{m}^{+}_{1} + \delta\mathbf{m}^{+}_{2}$ and $\delta\mathbf{m}^{-}_{1} + \delta\mathbf{m}^{-}_{2}$.

In Figs. 6(c) and 6(d), the ellipticities of $\delta\mathbf{m}^{+}_{1}$ and $\delta\mathbf{m}^{-}_{1}$ from each eigenfrequency branch are plotted, respectively. In each curve, positive (negative) ellipticity means right-handed (left-handed) elliptical polarization, and falls into the white (shaded) area. For magnonics in the SF phase, ellipticity of $\delta\mathbf{m}^{\pm}_{2}$ equals that of $\delta\mathbf{m}^{\pm}_{1}$, thus we have not provided them. We first focus on the hybridized pair: Ω_{I} and Ω_{III}. $\delta\mathbf{m}^{+}_{1}$ of Ω_{I} [red solid curve in Fig. 6(c)] changes from right-handed around $h = 0$ to linear polarized in $x'y$ plane at $h_{\mathrm{R}} \approx 2.170$ and then to left-handed until $h \to h^{\mathrm{FM}}$, while $\delta\mathbf{m}^{-}_{1}$ of Ω_{I} [red dashed curve in Fig. 6(d)] always keeps right-handed polarization for $h \in (0, h^{\mathrm{FM}})$. Alternatively, $\delta\mathbf{m}^{+}_{1}$ of Ω_{III} [cyan solid curve in Fig. 6(c)] is always right-handed polarized for $0 < h < h^{\mathrm{FM}}$. In particular, it tends to be linearly polarized in $\mathbf{e}_{z'}$ axis ($x'y$-plane) when $h \to 0$ ($h \to h^{\mathrm{FM}}$). As for $\delta\mathbf{m}^{-}_{1}$ of Ω_{III} [cyan dashed curve in Fig. 6(d)], it expands from linear polarization in the $x'y$ plane around $h = 0$ to right-handed and back to linear in the $x'y$ plane at $h = h_{\mathrm{R}}$, then becomes left-handed for $h_{\mathrm{R}} < h < h^{\mathrm{FM}}$, and finally becomes linearly polarized in the $\mathbf{e}_{z'}$ axis when $h \to h^{\mathrm{FM}}$. Across the whole region of $h \in (0, h^{\mathrm{FM}})$, the phase differences between $\delta\mathbf{m}^{+}_{1,2}$ for Ω_{I} and Ω_{III} remain π, while those between $\delta\mathbf{m}^{-}_{1,2}$ are 0. Next we turn to the other hybridized pair: Ω_{II} and Ω_{IV}. If we take the following correspondence: $\delta\mathbf{m}^{\pm}_{1}(\Omega_{\mathrm{I}}) \leftrightarrow \delta\mathbf{m}^{\mp}_{1}(\Omega_{\mathrm{II}})$ and $\delta\mathbf{m}^{\pm}_{1}(\Omega_{\mathrm{III}}) \leftrightarrow \delta\mathbf{m}^{\mp}_{1}(\Omega_{\mathrm{IV}})$, the same behaviors described above hold. The only difference is that the left-/right-hand transition point changes to $h_{\mathrm{L}} \approx 1.882$. At last, the spin-wave intensity ratio, $|\delta\mathbf{m}^{\pm}_{1}|^2/|\delta\mathbf{m}^{\pm}_{2}|^2$, always equals 1 for all frequency branches.

When p increases to 0.45, the magnoncis becomes more complicated and the main features are plotted in Fig. 7. Now the equilibrium magnetization layout falls in the MRS phase when $h \in [h_{\min}, h_{\max}]$ (shaded areas in all subfigures) with $h_{\min} = 3.034$ and $h_{\max} = 3.590$, leading to quite a few unique behaviors of spin waves. First, the four eigenfrequencies ($\Omega_{\mathrm{I\sim IV}}$) are provided in Fig. 7(a) by red, blue, cyan, and magenta solid curves in the order we have appointed while the $\Omega_1 \cup \Omega'_1$ and $\tilde{\Omega}_3 \cup \tilde{\Omega}'_3$ branches at $\psi = 0$ have been appended by orange and olive curves, respectively. We

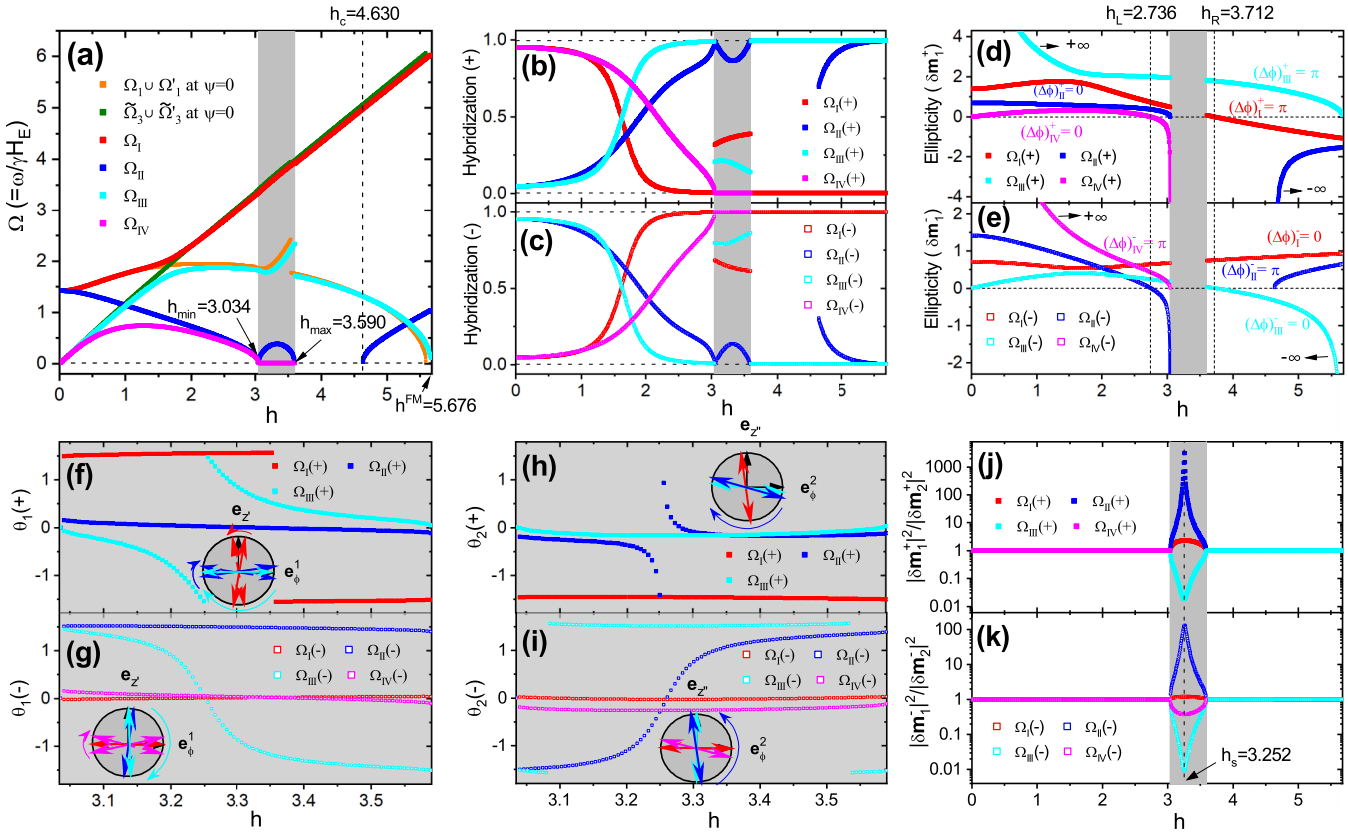

FIG. 7. Magnonics of symmetrical all-antiferromagnetic junctions with $k = 1$ and $p = 0.45$ under oblique dc fields with $\psi = \pi/10$. The equilibrium magnetization layout falls into the SF phase when $h \in (0, h_{\min}) \cup (h_{\max}, h^{\rm FM})$ and MRS phase when $h \in [h_{\min}, h_{\max}]$ (shaded area in all subfigures). (a) Four positive eigenfrequencies $\Omega_{\rm I}$ (red), $\Omega_{\rm II}$ (blue), $\Omega_{\rm III}$ (cyan), and $\Omega_{\rm IV}$ (magenta). The orange and olive curves are, respectively, $\Omega_1 \cup \Omega_1'$ and $\tilde{\Omega}_3 \cup \tilde{\Omega}_3'$ for $\psi = 0$ [see Fig. 5(a)]. (b), (c) Evolution of spin-wave intensities in subspaces with even and odd parities for all four eigenfrequencies. The parity operator for magnonics based on SF (MRS) phase is $\mathbb{C}$ ($\mathbb{M}_{xz}$). (d), (e) Ellipticities of $\delta\mathbf{m}_1^+$ and $\delta\mathbf{m}_1^-$ for all four SF-phase-based eigenfrequencies, which are identical to those of $\delta\mathbf{m}_2^\pm$. The corresponding phase differences between $\delta\mathbf{m}_{1,2}^\pm$ are indicated. (f), (g) Evolution of the linear polarization orientation of $\mathbf{l}_1^+$ and $\mathbf{l}_1^-$ for $h \in [h_{\min}, h_{\max}]$ based on MRS phase. (h), (i) Counterparts of (f) and (g) for $\mathbf{l}_2^+$ and $\mathbf{l}_2^-$. (j), (k) Intensity ratio of the spin-wave component of group 1 over that of group 2 in subspaces with even and odd parities under $\mathbb{C}$ ($\mathbb{M}_{xz}$) based on SF (MRS) phase.

have not provided the $\tilde{\Omega}_1 \cup \tilde{\Omega}_1'$ and $\Omega_3 \cup \Omega_3'$ branches in this subfigure since they are too close to $\Omega_{\rm II,IV}$. Similar to the $p < 1/4$ case, the original two interparity crossings in SF phase are lifted by oblique dc fields and become anticrossings. To confirm this, the weights in subspaces with even and odd parities (under $\mathbb{C}$) for each branch have been depicted in white areas of Figs. 7(b) and 7(c), respectively. Clearly, for $\Omega_{\rm I,IV}$ ($\Omega_{\rm II,III}$), $|\delta\mathbf{m}_1^+|^2 + |\delta\mathbf{m}_2^+|^2$ ($|\delta\mathbf{m}_1^-|^2 + |\delta\mathbf{m}_2^-|^2$) decreases from almost 1 to 0, indicating the hybridization of subspaces with opposite parities under $\mathbb{C}$. Spin waves in the SF phase are all elliptically polarized and the ellipticities of $\delta\mathbf{m}_1^\pm$ (equal to those of $\delta\mathbf{m}_2^\pm$) are, respectively, provided in Figs. 7(d) and 7(e), with positive (negative) values indicating right-handed (left-handed) polarization. Except for the MRS-phase-based shaded area, the details are quite similar to those in Figs. 6(c) and 6(d) of the $\psi = 0$ case, so we will not go into it again. The only difference is that $h_{\rm L,R}$ change to $h_{\rm L} = 2.736$ and $h_{\rm R} = 3.712$. In addition, the spin-wave intensity ratio always equals 1 for all branches in the SF phase, as shown in Figs. 7(j) and 7(k).

For spin waves in the MRS phase, the symmetry operator changes to $\mathbb{M}_{xz}$. Similar to in-plane-dc-field case, the $\pi/2$ phase difference between $\mathbf{l}_1^+ + \mathbf{l}_2^+$ and $\mathbf{l}_1^- + \mathbf{l}_2^-$ still exists. Except for this, the behaviors of spin waves become more fantastic. First, the weight distributions in the even and odd subspaces under $\mathbb{M}_{xz}$ are, respectively, plotted in the shaded areas in Figs. 7(b) and 7(c). For $\Omega_{\rm I,II,III}$, the spin wave spans the two subspaces. While for $\Omega_{\rm IV} = 0$, only the subspace with odd parity accommodates the spin wave. The polarization of all spin-wave components ($\mathbf{l}_{1,2}^\pm$) become linear. Figures 7(f) and 7(g) show the polarization directions for $\mathbf{l}_1^\pm$ in the local coordinate system ($\mathbf{e}_\phi^1$, $\mathbf{e}_{z'}$), which differ from those of $\mathbf{l}_2^\pm$ within ($\mathbf{e}_\phi^2$, $\mathbf{e}_{z''}$) presented in Figs. 7(h) and 7(i). Especially, as h increases from $h_{\min}$ to $h_{\max}$, $\mathbf{l}_1^+$ belonging to $\Omega_{\rm I}$, $\Omega_{\rm II}$ or $\Omega_{\rm III}$, respectively, swings around $\mathbf{e}_{z'}$, $\mathbf{e}_\phi^1$, or rotates clockwise from $+\mathbf{e}_\phi^1$ to $-\mathbf{e}_\phi^1$, as illustrated in Fig. 7(f). In contrast, Fig. 7(h) shows that $\mathbf{l}_2^+$ from $\Omega_{\rm I}$, $\Omega_{\rm III}$ or $\Omega_{\rm II}$, respectively, swings around $\mathbf{e}_{z''}$, $\mathbf{e}_\phi^2$, or rotates clockwise from $+\mathbf{e}_\phi^2$ to $-\mathbf{e}_\phi^2$. Their intensity ratios, $|\mathbf{l}_1^+|^2/|\mathbf{l}_2^+|^2$, are plotted in the shaded area in Fig. 7(j). Clearly, they all deviate from 1. In particular, $\mathbf{l}_2^+$ ($\mathbf{l}_1^+$) from $\Omega_{\rm II}$ ($\Omega_{\rm III}$) disappears at $h_{\rm s} = 3.252$. Then we move to the subspace with odd parity (under $\mathbb{M}_{xz}$). Now $\mathbf{l}_1^-$ belonging to $\Omega_{\rm I}$, $\Omega_{\rm IV}$, $\Omega_{\rm II}$, or $\Omega_{\rm III}$, respectively, swings around $\mathbf{e}_\phi^1$, $\mathbf{e}_\phi^1$, $\mathbf{e}_{z'}$,

or rotates clockwise from $+\mathbf{e}_{z'}$ to $-\mathbf{e}_{z'}$, as shown in Fig. 7(g) while Fig. 7(i) provides that $\mathbf{l}_2^-$ belonging to $\Omega_{\rm I}$, $\Omega_{\rm IV}$, $\Omega_{\rm III}$, or $\Omega_{\rm II}$, respectively, swings around $\mathbf{e}_\phi^2$, $\mathbf{e}_\phi^2$, $\mathbf{e}_{z''}$, or rotates anticlockwise from $-\mathbf{e}_{z''}$ to $+\mathbf{e}_{z''}$. At last, $|\mathbf{l}_1^-|^2/|\mathbf{l}_2^-|^2$ for all four branches are provided in Fig. 7(k). Again, $\mathbf{l}_2^-$ ($\mathbf{l}_1^-$) from $\Omega_{\rm II}$ ($\Omega_{\rm III}$) vanishes at $h_{\rm s} = 3.252$.

V. DISCUSSIONS AND CONCLUSION

First, in this paper the in-plane anisotropy has been neglected. This is applicable for two reasons. On one hand, in real symmetric all-antiferromagnetic junctions such as $Fe_2O_3/Cr_2O_3/Fe_2O_3$, the SF field of the spacers is much higher than that of the outermost Fe_2O_3 sublayers. Therefore, the neglect of in-plane anisotropy in Fe_2O_3 sublayers is acceptable. On the other hand, the easy-plane anistropy of Fe_2O_3 sublayers reduces the concomitant SF field $H_{\rm SF} \approx \sqrt{2H_E H_A}$ (H_A being the in-plane anisotropy field) to zero, which greatly simplifies our analytics and does not lose the most significant features of these junctions. Specifically, if we consider the in-plane anisotropy, the strict cruciferae state at $h = 0$ fails and the ground state should exhibit some kind of hysteresis behavior. SF and MRS phases will both survive, but the critical p should be larger than $1/4$ from the easy-plane case. The reason why we did not explore further is that the central vectorial equality like Eq. (6), which is the basis of our analytics, is hard to obtain. Hence the magnetization statics and corresponding magnonics can hardly be analyzed theoretically. However, the main features we have proposed in the main text should persist.

Second, the magnonics in the SF phase is relatively simple since the underlying symmetry operator is the polarization-preserved rotation ($\mathbb{C}_{2x}$ or $\mathbb{C}$). Spin waves therein are all elliptically polarized while bearing fixed phase differences between components both from subspaces with opposite parities and from the same subspace but different group (1 or 2). On the other hand, magnonics in the MRS phase is more interesting since now the underlying symmetry operator becomes the polarization-broken mirror reflection $\mathbb{M}_{xz}$. The most exciting feature is that oblique dc fields turn spin waves from elliptical to linear polarization. This can be understood by analogy to the superposition of two circularly polarized light with the same frequency but opposite rotation direction into linearly polarized light. In addition, the polarization direction of different components ($\mathbf{l}_{1,2}^{\pm}$) from various frequency branches ($\Omega_{\rm I\sim IV}$) experience a distinct swinging or rotating process in the transverse plane (of $\mathbf{m}_{A,1(2)}^{\rm eq}$) as the oblique dc field increases within the MRS phase. This provide a unique route of generating and manipulating linearly polarized spin waves in symmetric all-antiferromagnetic junctions.

Third, the emergence of the MRS phase relies on a relatively large intersublayer orthogonal coupling (in the easy-plane case, $p = H_p/H_E > 1/4$). In real all-antiferromagnetic junctions, this can be achieved by appropriately decreasing the spacer thickness or fine-tuning the nonuniform domain wall states in the spacers. In addition, the two outermost antiferromagnetic sublayers should be symmetric. If they are made of the same material but with different thickness, or just made of different materials, the MRS phase should fade out since generally $\mathbf{m}_{A(B),1(2)}^{\rm eq}$ cannot hold in the same latitude circle. $\mathbb{M}_{xz}$ is no longer the strict symmetry operator then the combined spin waves change from linear to elliptical polarization (although can be very narrow). Therefore, to efficiently generate and manipulate linearly polarized spin waves, the all-antiferromagnetic junctions should be precisely prepared as a symmetric configuration. Further investigations about the effects of asymmetry on magnetization statics and magnoncis should be also interesting but are beyond the scope of this paper.

In summary, by appropriately reformulating the orthogonal coupling in Eq. (2), in this paper the equilibrium magnetization layout and the corresponding coherent magnonics in symmetric all-antiferromagnetic junctions are systematically revealed. Our contribution is mainly focused on three aspects: (i) Under strong enough orthogonal coupling, the equilibrium magnetization layout can fall into the MRS phase, which is quite different from the usual SF phase that antiferromagnets often experience. (ii) For in-plane dc fields, two interparity and two intraparity accidental crossings exist in the eigenfrequency spectrum of spin waves in the SF phase. At $h = h_{\rm min}$ ($h_{\rm max}$), where a second-order (first-order) PT occurs between SF and MRS phases, eigenfrequencies are continuous (discontinuous). Except for some isolated special points ($h_{\rm min}$, $h_{\rm max}$ and $h_{\rm c}$), spin waves are always elliptically polarized for $h \in (0, h^{\rm FM})$. (iii) Oblique dc fields turn the interparity crossings in the SF phase into anticrossings while inducing considerable hybridization between elliptically polarized spin-wave components belonging to subspaces with even and odd parities. The most exciting progress resides in magnonics based on the MRS phase, which is defined upon $\mathbb{M}_{xz}$. The spin-wave components become linearly polarized and the polarization direction can be fine controlled by field strength within MRS phase. Our results lay the foundation for magnetic phases and the corresponding coherent magnonics in symmetric all-antiferromagnetic junctions while opening an avenue for magnetic nanodevices with ultrahigh density and ultrafine control of magnonics.

ACKNOWLEDGMENTS

M.L. acknowledges supports from the National Natural Science Foundation of China (Grant No. 12204403). B.X. is funded by the National Natural Science Foundation of China (Grant No. 11774300). W.H. is supported by the National Natural Science Foundation of China (Grant No. 12174427).

APPENDIX A: EXPLICIT FORM OF THE QUARTIC EQUATION IN SEC. IV C

The parameters $J_{0,1,2,3}$ in the quartic algebraic equation of Ω^2: $(\Omega^2)^4 + J_3(\Omega^2)^3 + J_2(\Omega^2)^2 + J_1(\Omega^2) + J_0 = 0$ has the following explicit form:

$$
\begin{aligned}
J_0 &= [(e_1)^2 - (e_2)^2][(f_1)^2 - (f_2)^2],\\
J_1 &= 2(e_2 f_2 - e_1 f_1)[(a_1 + a_2)(b_2 + c_2) + (a_1 - a_2)\\
&\quad (b_1 - c_1)] + 2(e_2 f_1 - e_1 f_2)[(a_1 + a_2)(b_1 - c_1)\\
&\quad + (a_1 - a_2)(b_2 + c_2)] + 2e_1[(f_1)^2 - (f_2)^2]\\
&\quad + 2f_1[(e_1)^2 - (e_2)^2],
\end{aligned}
$$

$$
\begin{aligned}
J_2 &= [(e_1+f_1)-(a_1+a_2)(b_2+c_2)-(a_1-a_2)(b_1-c_1)]^2 \\
&\quad -[(e_2-f_2)-(a_1+a_2)(b_1-c_1)-(a_1-a_2) \\
&\quad (b_2+c_2)]^2+2(e_1f_1-e_2f_2), \\
J_3 &= 2[(e_1+f_1)-(a_1+a_2)(b_2+c_2)-(a_1-a_2)(b_1-c_1)],
\end{aligned}
\tag{A1}
$$

with

$$
\begin{aligned}
a_1 &= 1-4p\cos^2\epsilon, \\
a_2 &= 1+4p\cos^2\epsilon, \\
b_1 &= 1+2p\sin^2 2\epsilon-4p\cos^2\epsilon\cos 2\epsilon+k\sin^2\epsilon\sin^2\chi, \\
b_2 &= \cos 2\epsilon-2p\sin^2 2\epsilon-4p\cos^2\epsilon, \\
c_1 &= 1+4p\cos^2\epsilon\cos 2\epsilon+k\sin^2\epsilon\sin^2\chi, \\
c_2 &= \cos 2\epsilon+4p\cos^2\epsilon, \\
d &= \frac{k}{2}\sin\epsilon\sin 2\chi, \\
e_1 &= a_2(b_2-b_1)-kb_1\cos^2\chi+d^2, \\
e_2 &= a_2(b_1-b_2)-kb_2\cos^2\chi \\
f_1 &= a_1(c_2-c_1)-kc_1\cos^2\chi+d^2, \\
f_2 &= a_1(c_1-c_2)-kc_2\cos^2\chi.
\end{aligned}
\tag{A2}
$$

APPENDIX B: DETAILED P_{MRS} UNDER OBLIQUE DC FIELDS

After defining $\tilde{p}\equiv p[(\mathbf{m}^{\mathrm{eq}}_{A,1}+\mathbf{m}^{\mathrm{eq}}_{A,2})(\mathbf{m}^{\mathrm{eq}}_{B,1}+\mathbf{m}^{\mathrm{eq}}_{B,2})]=p\{\sin^2\theta_1[(\cos\phi_1+\cos\phi_2)^2-(\sin\phi_1-\sin\phi_2)^2]+4\cos^2\theta_1\}$, $\mu\equiv\sin\eta\cos\epsilon-\sin\theta_1\cos\phi_2\cos\chi(1+\tan\chi\tan\xi)\sin\epsilon-\sin 2\epsilon$, $\nu\equiv\sin 2\eta+\sin\theta_1\cos\phi_1\cos\xi(1+\tan\chi\tan\xi)\sin\eta-\sin\epsilon\cos\eta$, and $\kappa\equiv\sin\theta_1(\cos\phi_2-\cos\phi_1)$, the elements of $\tilde{\Theta}$ and $\tilde{\Phi}$ from P_{MRS} in Eq. (29) are as follows:

$$
\begin{aligned}
\tilde{\Theta}_{11} &= -\mathrm{i}k\sin\epsilon\sin\chi\cos\chi, \\
\tilde{\Theta}_{12} &= -\mathrm{i}(\tilde{p}-1)\sin\eta\sin(\xi-\chi), \\
\tilde{\Theta}_{13} &= 1-\tilde{p}+k\cos^2\chi, \\
\tilde{\Theta}_{14} &= (1-\tilde{p})\cos(\xi-\chi), \\
\tilde{\Theta}_{21} &= -\mathrm{i}(\tilde{p}-1)\sin\epsilon\sin(\xi-\chi), \\
\tilde{\Theta}_{22} &= \mathrm{i}k\sin\eta\sin\xi\cos\xi, \\
\tilde{\Theta}_{23} &= \tilde{\Theta}_{14}, \\
\tilde{\Theta}_{24} &= 1-\tilde{p}+k\cos^2\xi, \\
\tilde{\Theta}_{31} &= \tilde{p}\cos 2\epsilon+1+k\sin^2\epsilon\sin^2\chi, \\
\tilde{\Theta}_{32} &= (\tilde{p}+1)\cos\epsilon\cos\eta \\
&\quad +(\tilde{p}-1)\sin\epsilon\sin\eta\cos(\xi-\chi), \\
\tilde{\Theta}_{33} &= -\tilde{\Theta}_{11}, \\
\tilde{\Theta}_{34} &= -\tilde{\Theta}_{21}, \\
\tilde{\Theta}_{41} &= \tilde{\Theta}_{32}, \\
\tilde{\Theta}_{42} &= \tilde{p}\cos 2\eta+1+k\sin^2\eta\sin^2\xi, \\
\tilde{\Theta}_{43} &= -\tilde{\Theta}_{12}, \\
\tilde{\Theta}_{44} &= -\tilde{\Theta}_{22}
\end{aligned}
\tag{B1}
$$

and

$$
\begin{aligned}
\tilde{\Phi}_{11} &= -\mathrm{i}k\sin\epsilon\sin\chi\cos\chi-2\mathrm{i}p\mu\kappa\sin\chi, \\
\tilde{\Phi}_{12} &= \mathrm{i}(\tilde{p}+1)\sin\eta\sin(\xi-\chi)-2\mathrm{i}p\nu\kappa\sin\chi, \\
\tilde{\Phi}_{13} &= (\tilde{p}+1+k\cos^2\chi)+2p\kappa^2\sin^2\chi, \\
\tilde{\Phi}_{14} &= (\tilde{p}+1)\cos(\xi-\chi)-2p\kappa^2\sin\chi\sin\xi, \\
\tilde{\Phi}_{21} &= \mathrm{i}(\tilde{p}+1)\sin\epsilon\sin(\xi-\chi)+2\mathrm{i}p\mu\kappa\sin\xi, \\
\tilde{\Phi}_{22} &= \mathrm{i}k\sin\eta\sin\xi\cos\xi+2\mathrm{i}p\kappa\nu\sin\xi, \\
\tilde{\Phi}_{23} &= \tilde{\Phi}_{14}, \\
\tilde{\Phi}_{24} &= (\tilde{p}+1+k\cos^2\xi)+2p\kappa^2\sin^2\xi, \\
\tilde{\Phi}_{31} &= (1+k\sin^2\epsilon\sin^2\chi-\tilde{p}\cos 2\epsilon)+2p\mu^2, \\
\tilde{\Phi}_{32} &= 2p\mu\nu+(1-\tilde{p})\cos\epsilon\cos\eta \\
&\quad -(1+\tilde{p})\sin\epsilon\sin\eta\cos(\xi-\chi), \\
\tilde{\Phi}_{33} &= -\tilde{\Phi}_{11}, \\
\tilde{\Phi}_{34} &= -\tilde{\Phi}_{21}, \\
\tilde{\Phi}_{41} &= \tilde{\Phi}_{32}, \\
\tilde{\Phi}_{42} &= (1+k\sin^2\eta\sin^2\xi-\tilde{p}\cos 2\eta)+2p\nu^2, \\
\tilde{\Phi}_{43} &= -\tilde{\Phi}_{12}, \\
\tilde{\Phi}_{44} &= -\tilde{\Phi}_{22}.
\end{aligned}
\tag{B2}
$$

[1] Y. Zhou, L. Liao, T. Guo, H. Bai, M. Zhao, C. Wan, L. Huang, L. Han, L. Qiao, Y. You, C. Chen, R. Chen, Z. Zhou, X. F. Han, F. Pan, and C. Song, Nat. Commun. **13**, 3723 (2022).

[2] R. A. Duine, K.-J. Lee, S. S. P. Parkin, and M. D. Stiles, Nat. Phys. **14**, 217 (2018).

[3] T. Martin, M. Belmeguenai, M. Maier, K. Perzlmaier, and G. Bayreuther, J. Appl. Phys. **101**, 09C101 (2007).

[4] M. Belmeguenai, T. Martin, G. Woltersdorf, G. Bayreuther, V. Baltz, A. K. Suszka, and B. J. Hickey, J. Phys.: Condens. Matter **20**, 345206 (2008).

[5] T. Seki, H. Tomita, A. A. Tulapurkar, M. Shiraishi, T. Shinjo, and Y. Suzuk, Appl. Phys. Lett. **94**, 212505 (2009).

[6] D. E. Gonzalez-Chavez, R. Dutra, W. O. Rosa, T. L. Marcondes, A. Mello, and R. L. Sommer, Phys. Rev. B **88**, 104431 (2013).

[7] A. A. Timopheev, Y. G. Pogorelov, S. Cardoso, P. P. Freitas, G. N. Kakazei, and N. A. Sobolev, Phys. Rev. B **89**, 144410 (2014).

[8] X. M. Liu, H. T. Nguyen, J. Ding, M. G. Cottam, and A. O. Adeyeye, Phys. Rev. B **90**, 064428 (2014).

[9] K. Tanaka, T. Moriyama, M. Nagata, T. Seki, K. Takanashi, S. Takahashi, and T. Ono, Appl. Phys. Express **7**, 063010 (2014).

[10] H. Yang, Y. Li, and W. E. Bailey, Appl. Phys. Lett. **108**, 242404 (2016).

[11] S. Li, Q. Li, J. Xu, S. Yan, G.-X. Miao, S. Kang, Y. Dai, J. Jiao, and Y. Lü, Adv. Funct. Mater. **26**, 3738 (2016).

[12] C. Wang, S. Zhang, S. Qiao, H. Du, X. Liu, R. Sun, X.-M. Chu, G.-X. Miao, Y. Dai, S. Kang, S. Yan, and S. Li, Appl. Phys. Lett. **112**, 192401 (2018).

[13] W. Wang, P. Li, C. Cao, F. Liu, R. Tang, G. Chai, and C. Jiang, Appl. Phys. Lett. **113**, 042401 (2018).

[14] W. J. Kong, C. H. Wan, B. S. Tao, C. Fang, L. Huang, C. Y. Guo, M. Irfan, and X. F. Han, Appl. Phys. Lett. **113**, 162402 (2018).

[15] A. Kamimaki, S. Iihama, T. Taniguchi, and S. Mizukami, Appl. Phys. Lett. **115**, 132402 (2019).

[16] R. Y. Chen, R. Q. Zhang, L. Y. Liao, X. Z. Chen, Y. J. Zhou, Y. D. Gu, M. S. Saleem, X. F. Zhou, F. Pan, and C. Song, Appl. Phys. Lett. **115**, 132403 (2019).

[17] S. Sorokin, R. A. Gallardo, C. Fowley, K. Lenz, A. Titova, G. Y. P. Atcheson, G. Dennehy, K. Rode, J. Fassbender, J. Lindner, and A. M. Deac, Phys. Rev. B **101**, 144410 (2020).

[18] A. Kamimaki, S. Iihama, K. Z. Suzuki, N. Yoshinaga, and S. Mizukami, Phys. Rev. Appl. **13**, 044036 (2020).

[19] Y. Shiota, T. Taniguchi, M. Ishibashi, T. Moriyama, and T. Ono, Phys. Rev. Lett. **125**, 017203 (2020).

[20] M. Ishibashi, Y. Shiota, T. Li, S. Funada, T. Moriyama, and T. Ono, Sci. Adv. **6**, eaaz6931 (2020).

[21] A. Sud, C. W. Zollitsch, A. Kamimaki, T. Dion, S. Khan, S. Iihama, S. Mizukami, and H. Kurebayashi, Phys. Rev. B **102**, 100403(R) (2020).

[22] H. J. Waring, N. A. B. Johansson, I. J. Vera-Marun, and T. Thomson, Phys. Rev. Appl. **13**, 034035 (2020).

[23] M. Li, J. Lu, and W. He, Phys. Rev. B **103**, 064429 (2021).

[24] W. He, Z. K. Xie, R. Sun, M. Yang, Y. Li, X.-T. Zhao, W. Liu, Z. D. Zhang, J.-W. Cai, Z.-H. Cheng, and J. Lu, Chinese Phys. Lett. **38**, 057502 (2021).

[25] R. E. Troncoso, M. A. Lund, A. Brataas, and A. Kamra, Phys. Rev. B **103**, 144422 (2021).

[26] C. Dai and F. Ma, Appl. Phys. Lett. **118**, 112405 (2021).

[27] X. Chen, C. Zheng, S. Zhou, Y. Liu, and Z. Zhang, J. Phys.: Condens. Matter **34**, 015802 (2022).

[28] M. A. Ruderman and C. Kittel, Phys. Rev. **96**, 99 (1954).

[29] Y. Yafet, J. Appl. Phys. **61**, 4058 (1987).

[30] P. Bruno and C. Chappert, Phys. Rev. Lett. **67**, 1602 (1991).

[31] H. Nakayama, M. Althammer, Y.-T. Chen, K. Uchida, Y. Kajiwara, D. Kikuchi, T. Ohtani, S. Geprägs, M. Opel, S. Takahashi, R. Gross, G. E. W. Bauer, S. T. B. Goennenwein, and E. Saitoh, Phys. Rev. Lett. **110**, 206601 (2013).

[32] Y.-T. Chen, S. Takahashi, H. Nakayama, M. Althammer, S. T. B. Goennenwein, E. Saitoh, and G. E. W. Bauer, Phys. Rev. B **87**, 144411 (2013).

[33] G. R. Hoogeboom, A. Aqeel, T. Kuschel, T. T. M. Palstra, and B. J. van Wees, Appl. Phys. Lett. **111**, 052409 (2017).

[34] Y. Cheng, S. Yu, A. S. Ahmed, M. Zhu, Y. Rao, M. Ghazisaeidi, J. Hwang, and F. Yang, Phys. Rev. B **100**, 220408(R) (2019).

[35] J. Fischer, M. Althammer, N. Vlietstra, H. Huebl, S. T. B. Goennenwein, R. Gross, S. Geprägs, and M. Opel, Phys. Rev. Appl. **13**, 014019 (2020).

[36] S. K. Kim, Y. Tserkovnyak, and O. Tchernyshyov, Phys. Rev. B **90**, 104406 (2014).

[37] S. Dasgupta and O. Tchernyshyov, Phys. Rev. B **102**, 144417 (2020).

[38] S. Dasgupta and J. Zou, Phys. Rev. B **104**, 064415 (2021).

[39] T. L. Gilbert, IEEE Trans. Magn. **40**, 3443 (2004).

[40] F. B. Anderson and H. B. Callen, Phys. Rev. **136**, A1068 (1964).

[41] E. S. Dayhoff, Phys. Rev. **107**, 84 (1957).

[42] S. Foner, Phys. Rev. **130**, 183 (1963).

[43] R. Lebrun, A. Ross, O. Gomonay, V. Baltz, U. Ebels, A.-L. Barra, A. Qaiumzadeh, A. Brataas, J. Sinova, and M. Kläui, Nat. Commun. **11**, 6332 (2020).

[44] J. Han, P. Zhang, Z. Bi, Y. Fan, T. S. Safi, J. Xiang, J. Finley, L. Fu, R. Cheng, and L. Liu, Nat. Nanotechnol. **15**, 563 (2020).

[45] S. Saito, M. Miura, and K. Kurosawa, J. Phys. C: Solid State Phys. **13**, 1513 (1980).

[46] K. Kurosawa, M. Miura, and S. Saito, J. Phys. C: Solid State Phys. **13**, 1521 (1980).

[47] H. Y. Yuan and R. A. Duine, Phys. Rev. B **103**, 134440 (2021).